



1 Earth System Model Aerosol-Cloud Diagnostics Package 2 (ESMAC Diags) Version 1: Assessing E3SM Aerosol Predictions 3 Using Aircraft, Ship, and Surface Measurements

4 Shuaiqi Tang¹, Jerome D. Fast¹, Kai Zhang¹, Joseph C. Hardin², Adam C. Varble¹, John E.
5 Shilling¹, Fan Mei¹, Maria A. Zawadowicz³ and Po-Lun Ma¹

6 ¹Pacific Northwest National Laboratory, Richland, WA, USA

7 ²ClimateAI Inc, San Francisco, CA, USA

8 ³Brookhaven National Laboratory, Upton, NY, USA

9 *Correspondence to:* Shuaiqi Tang (shuaiqi.tang@pnnl.gov)

10

11 **Abstract.** An Earth System Model (ESM) aerosol-cloud diagnostics package is developed to facilitate the
12 routine evaluation of aerosols, clouds and aerosol-cloud interactions simulated by the Department of
13 Energy's (DOE) Energy Exascale Earth System Model (E3SM). The first version focuses on comparing
14 simulated aerosol properties with aircraft, ship, and surface measurements, most of them are measured in-
15 situ. The diagnostics currently covers six field campaigns in four geographical regions: Eastern North
16 Atlantic (ENA), Central U.S. (CUS), Northeastern Pacific (NEP) and Southern Ocean (SO). These
17 regions produce frequent liquid or mixed-phase clouds with extensive measurements available from the
18 Atmospheric Radiation Measurement (ARM) program and other agencies. Various types of diagnostics
19 and metrics are performed for aerosol number, size distribution, chemical composition, CCN
20 concentration and various meteorological quantities to assess how well E3SM represents observed aerosol
21 properties across spatial scales. Overall, E3SM qualitatively reproduces the observed aerosol number
22 concentration, size distribution and chemical composition reasonably well, but underestimates Aitken
23 mode and overestimates accumulation mode aerosols over the CUS region, and underestimates aerosol
24 number concentration over the SO region. The current version of E3SM struggles to reproduce new
25 particle formation events frequently observed over both the CUS and ENA regions, indicating missing
26 processes in current parameterizations. The diagnostics package is coded and organized in a way that can
27 be easily extended to other field campaign datasets and adapted to higher-resolution model simulations.
28 Future releases will include comprehensive cloud and aerosol-cloud interaction diagnostics.

29



30 1. Introduction

31 Aerosol number, mass, size, composition, and mixing state affect how aerosol populations scatter and
32 absorb solar radiation and influence cloud albedo, amount, lifetime, and precipitation (Twomey, 1977;
33 Albrecht, 1989) by acting as cloud condensation nuclei (e.g., Petters and Kreidenweis, 2007). However,
34 there are still knowledge and measurement gaps on the physical and chemical mechanisms regulating the
35 sources, sinks, gas-to-particle partitioning (e.g., secondary formation processes), and spatiotemporal
36 distribution of aerosol populations. Consequently, the representation of the aerosol lifecycle and the
37 interaction of aerosol populations with clouds and radiation in Earth system models (ESMs) still suffer
38 from large uncertainties (Seinfeld et al., 2016; Carslaw et al., 2018), which impacts the ability of ESMs to
39 predict the evolution of the climate system (IPCC, 2013).

40 To facilitate model evaluation and document the performance of parameterizations in ESMs, many
41 modeling centers have developed standardized diagnostics packages. Some examples focus on
42 meteorological metrics include the U.S. National Center of Atmospheric Research (NCAR) Atmospheric
43 Model Working Group (AMWG) diagnostics package (AMWG, 2021), the U.S. Department of Energy
44 (DOE) Energy Exascale Earth System Model (E3SM, Golaz et al., 2019) diagnostics (E3SM, 2021), the
45 European Union (EU) Earth System Model Evaluation Tool (ESMValTool, Eyring et al., 2016), and the
46 Program for Climate Model Diagnosis and Intercomparison (PCMDI) Metric Package (PMP, Gleckler et
47 al., 2016). Some recent efforts focus on process-oriented diagnostics (POD) that are designed to provide
48 insights into parameterization developments to address long-standing model biases. Maloney et al. (2019)
49 summarizes the activities by the U.S. National Oceanic and Atmospheric Administration (NOAA)
50 Modeling, Analysis, Prediction, and Projections program (MAPP) Model Diagnostics Task Force
51 (MDTF) to apply community-developed PODs to climate and weather prediction models. Zhang et al.
52 (2020) developed a diagnostics package that utilizes statistics derived from long-term ground-based
53 measurements from the DOE Atmospheric Radiation Measurement (ARM) User Facility for climate
54 model evaluation. Aerosol properties, however, are not included in these diagnostics packages.

55 The international collaborative AeroCom project (Myhre et al., 2013; Schulz et al., 2006) focuses on
56 evaluation of aerosol predictions using available measurements and includes intercomparisons among
57 global models to assess uncertainties in seasonal and regional variations in aerosol properties and their
58 potential impact on climate. Their diagnostics heavily rely on satellite remote sensing products (e.g.,
59 aerosol optical depth) which have global coverage but poor spatial and temporal resolution that hinders a
60 process-level understanding of the sources of model uncertainty. More recently, the Global Aerosol
61 Synthesis and Science Project (GASSP, Reddington et al., 2017; Watson-Parris et al., 2019) has
62 developed a global database of aerosol observations from fixed surface sites as well as ship and aircraft



63 platforms from 86 field campaigns between 1990 and 2015 that can be used for model evaluation. Recent
64 field campaigns after year 2015 are not included in this effort.

65 Many aerosol properties are difficult to measure directly. Remote sensing instruments (e.g., ground
66 and satellite radiometers) that only measure radiative properties of column-integrated aerosols, such as
67 optical depth, are frequently used to evaluate model predictions. Instruments such as ground lidars (e.g.,
68 Campbell et al., 2002) or lidars onboard aircraft (e.g., Müller et al., 2014) and satellite (e.g., CALIPSO,
69 Winker et al., 2009) platforms can provide vertical profiles of aerosol extinction, backscatter, and/or
70 depolarization, but they do not directly measure aerosol number, size and composition. Therefore, the
71 quantities measured by remote sensing instruments cannot be used alone to assess model predictions of
72 aerosol-radiation-cloud-precipitation interactions. Surface monitoring sites provide long-term in situ
73 aerosol property measurements but are limited to land locations with far fewer operational sites compared
74 to those dedicated to routine meteorological sampling. Ship and aircraft platforms are commonly
75 deployed during field campaigns to obtain in situ and remote sensing aerosol property measurements in
76 remote or poorly sampled locations such as over the ocean and within the free troposphere, which are
77 highly valuable when studying spatial variations of aerosols. Aircraft platforms also provide a means to
78 obtain coincident measurements of aerosol and cloud properties needed to understand their interactions.
79 Although in-situ ship and airborne aerosol measurements are usually limited to specific locations for short
80 time periods, the increasing number of completed field campaigns conducted over a range of atmospheric
81 conditions provides an opportunity to use them for model evaluation.

82 As noted by Reddington et al. (2017), the considerable investment in collecting field campaign
83 measurements of aerosol properties is underexploited by the climate modeling community. This can be
84 largely attributed to datasets located in disparate repositories and the lack of a standardized file format
85 that requires excessive time and effort spent on manipulating the datasets to facilitate comparisons
86 between observed and simulated values, especially for those unfamiliar with measurement techniques,
87 assumptions, and uncertainties. With many field campaigns conducted since 2015 being available but
88 rarely used for model evaluation, this study describes the first version of the ESM Aerosol-Cloud
89 Diagnostics (ESMAC Diags) package to facilitate the evaluation of ESM-predicted aerosols, utilizing
90 recent measurements from aircraft, ship and surface platforms collected by the U.S. DOE ARM and
91 National Science Foundation (NSF) NCAR user facilities, most of which are in-situ measurements. The
92 overall structure of ESMAC Diags is designed similar to the Aerosol Modeling Testbed for the Weather
93 Research and Forecasting (WRF) model described in Fast et al. (2011), except that it uses Python to
94 interface the measurements with ESM output and does not preprocess the observational dataset into a
95 common format. The diagnostics package is firstly designed with and applied to E3SM Atmosphere



96 Model version 1 (EAMv1, Rasch et al., 2019). EAMv1 uses an improved modal aerosol treatment
97 implemented based on the 4-mode version of the modal aerosol module (MAM4, Liu et al., 2016), such
98 as improved treatment of H₂SO₄ vapor for new particle formation, improved SOA treatment, new MOA
99 species, improvements to aerosol convective transport, wet removal, resuspension from evaporation and
100 aerosol-affected cloud microphysical processes (Wang et al., 2020). Only minimal modifications to the
101 diagnostics package are needed for potential application to other ESMs.

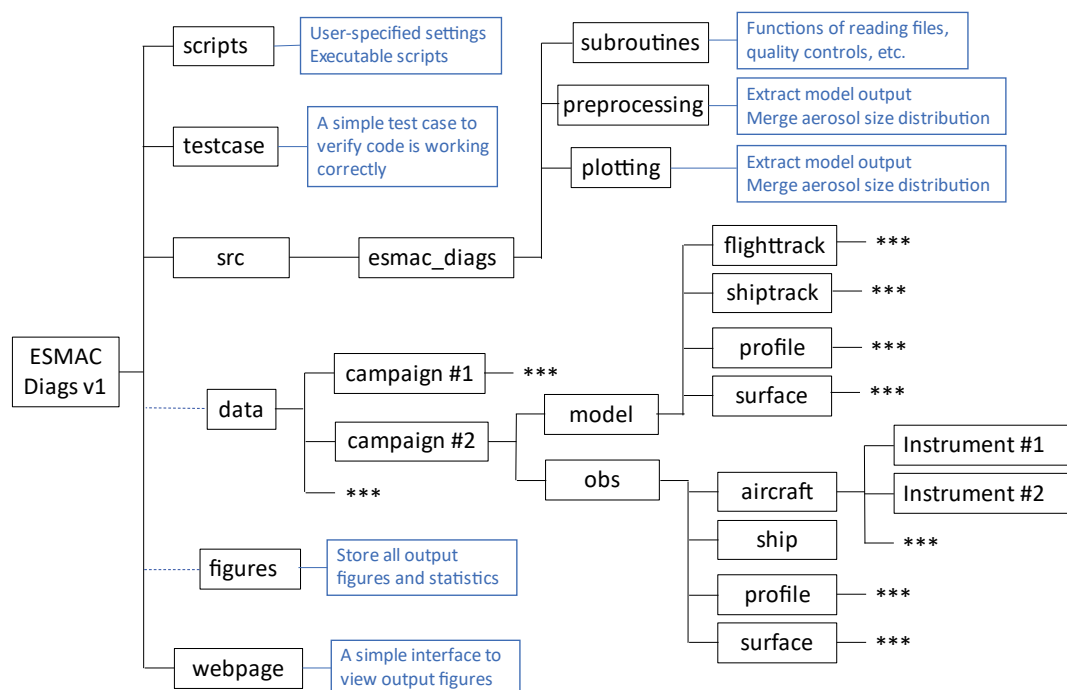
102

103 **2. Introduction of ESMAC Diags**

104 The diagnostics package is designed to be flexible so that additional measurements and functionality can
105 be included in the future. The workflow of ESMAC Diags, illustrated in Figure 1, consists of six major
106 components. The “scripts” directory contains executable scripts and user-specified settings. The “src”
107 directory contains all source code including code used to preprocess model output, read files, merge
108 measurements from different instruments, compute observed versus simulated statistical relationships,
109 and plot results. All observational and model data in the “data” directory are organized by field campaign.
110 The diagnostic plots and statistics are put in the “figures” directory, also organized by field campaign.
111 The “testcase” directory includes a small amount of input and verify data to test if the package is installed
112 properly. The “webpage” directory provides an interface to view diagnostics figures. It is relatively
113 straightforward to add other field campaigns or datasets using this structure. Most of the datasets used in
114 ESMAC Diags are in a standardized netCDF format (NETCDF, 2021); however, some ARM aircraft
115 measurements use different ASCII formats. Currently, the diagnostic package reads observational data
116 directly from their original format. In the long term, we may standardize the observational data format in
117 a similar manner as was done in GASSP project (Reddington et al., 2017).



118



119

120 **Figure 1: Workflow of ESMAC Diags. Boxes in blue describe the functions of the directory.**
 121 **Asterisks represent boxes that follow the same format as those shown in parallel.**

122 **2.1 Field observations and merged aerosol size distribution**

123 We initially focus on four geographical regions where liquid clouds occur frequently and extensive
 124 measurements are available from ARM and other agencies: Eastern North Atlantic (ENA), Northeastern
 125 Pacific (NEP), Central U.S. (CUS, where the ARM Southern Great Plains, SGP, site is located), and
 126 Southern Ocean (SO). Aerosol properties also vary among these regions. Six field campaigns from these
 127 four testbeds are selected in the version 1.0 of ESMAC Diags (Table 1). HI-SCALE and ACE-ENA are
 128 based on long-term ARM ground sites with aircraft field campaigns sampling below, within, and above
 129 convective and marine boundary layer clouds, respectively, within a few hundred kilometers around the
 130 sites. CSET and MAGIC are field campaigns with aircraft and ship platforms, respectively, sampling
 131 transects between California and Hawaii characterized by a transition between stratocumulus and trade
 132 cumulus dominated regions. SOCRATES and MARCUS are field campaigns with aircraft and ship
 133 platforms, respectively, based out of Hobart, Australia. Aircraft transects during SOCRATES extended

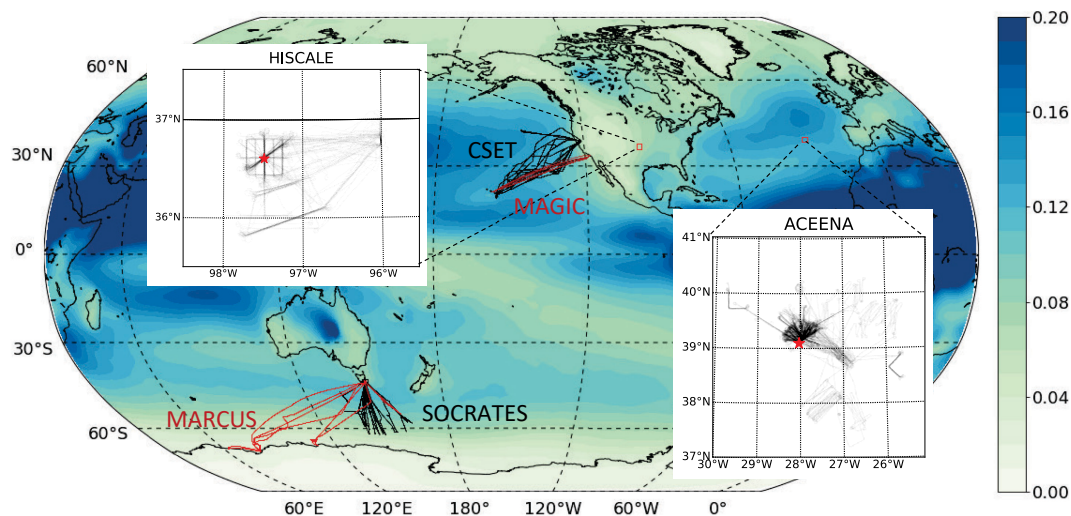


134 south to around 60°S, while ship transects during MARCUS extended southwest from Hobart to
 135 Antarctica. The aircraft (black) and ship (red) tracks for these field campaigns are shown in Figure 2.

136 **Table 1. Descriptions of the field campaigns used in this study. Numbers after aircraft or ship**
 137 **represent number of flights or ship trips in each field campaign or IOP.**

Campaign*	Period	Platform	Typical Conditions	Reference
HI-SCALE	IOP1: 24 Apr – 21 May 2016 IOP2: 28 Aug – 24 Sep 2016	Ground, aircraft (IOP1: 17, IOP2: 21)	Continental cumulus with high aerosol loading	(Fast et al., 2019)
ACE-ENA	IOP1: 21 Jun – 20 Jul 2017 IOP2: 15 Jan – 18 Feb 2018	Ground, aircraft (IOP1: 20, IOP2: 19)	Marine stratocumulus with low aerosol loading	(Wang et al., 2021)
MAGIC	Oct 2012 – Sep 2013	Ship (18)	Marine stratocumulus to cumulus transition with low aerosol loading	(Lewis and Teixeira, 2015; Zhou et al., 2015)
CSET	1 Jul – 15 Aug 2015	Aircraft (16)	Same as above	(Albrecht et al., 2019)
MARCUS	Oct 2017 – Apr 2018	Ship (4)	Marine liquid and mixed phase clouds with low aerosol loading	(McFarquhar et al., 2021)
SOCRATES	15 Jan – 24 Feb, 2018	Aircraft (14)	Same as above	(McFarquhar et al., 2021)

138 * full names of the listed field campaigns:
 139 HI-SCALE: Holistic Interactions of Shallow Clouds, Aerosols and Land Ecosystems
 140 ACE-ENA: Aerosol and Cloud Experiments in the Eastern North Atlantic
 141 MAGIC: Marine ARM GCSS Pacific Cross-section Intercomparison (GPCI) Investigation of Clouds
 142 CSET: Cloud System Evolution in the Trades
 143 MARCUS: Measurements of Aerosols, Radiation and Clouds over the Southern Ocean
 144 SOCRATES: Southern Ocean Cloud Radiation and Aerosol Transport Experimental Study
 145



146
 147

148 **Figure 2. Aircraft (black) and ship (red) tracks for the six field campaigns. Overlaid is aerosol**
 149 **optical depth at 550nm averaged from 2014 to 2018 simulated in EAMv1.**

150 The instruments and measurements used in ESMAC Diags version 1.0 are listed in Table 2. Note that
 151 some instruments are only available for certain field campaigns or failed operationally during certain
 152 periods, so that model evaluation is limited by the availability of data collected in each field campaign.
 153 ARM data usually include quality flags indicating bad or indeterminate data. These flagged data are
 154 filtered out, except surface CPC measurements for HI-SCALE, that data flagged as greater than maximum
 155 value (8000 cm^{-3}) are retained since aerosol loading can be higher than that during new particle formation
 156 events. This exception ensures a reasonable diurnal cycle shown in Section 3.3. For some data that do not
 157 have a quality flag (e.g., UHSAS data in NCAR research flight measurements), a simple minimum and
 158 maximum threshold is applied. For some field campaigns (HI-SCALE and ACE-ENA), there are several
 159 instruments (e.g., FIMS, PCASP, OPC for aircraft; SMPS and nanoSMPS for ground) measuring aerosol
 160 size distribution over different size ranges. These datasets are merged to create a more complete size
 161 distribution. The aerosol concentrations in the “overlapping” bins measured by multiple instruments are
 162 weighted by the uncertainty of each instrument based on the knowledge of the ARM instrument mentors.
 163 An example of the merged aerosol size distribution and individual measurements for one flight in ACE-
 164 ENA is shown in Figure 3. Ranging from 10^1 to 10^4 nm, the merged aerosol size distribution data account
 165 for ultrafine, Aitken, and accumulation modes.

166 **Table 2. List of instruments and measurements used in ESMAC Diags v1.0.**

Instrument	Platform	Measurements	Available campaigns	DOIs or References
------------	----------	--------------	---------------------	--------------------

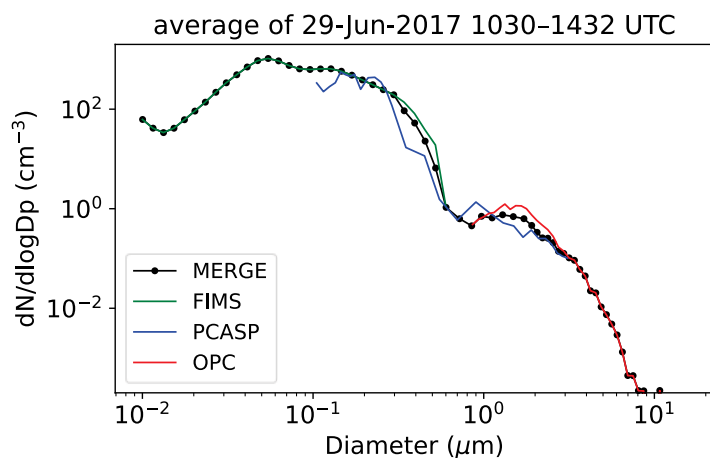


Surface meteorological station (MET)	Ground, ship	Temperature, relative humidity, wind, pressure	HI-SCALE, ACE-ENA, MAGIC, MARCUS	HI-SCALE, ACE-ENA: (Kyrouac and Shi, 2018) MAGIC: (ARM, 2014) MARCUS: 10.5439/1593144
Scanning mobility particle sizer (SMPS)	Ground	Aerosol size distribution (20–700 nm)	HI-SCALE	(Howie and Kuang, 2016)
Nano scanning mobility particle sizer (nanoSMPS)	Ground	Aerosol size distribution (2–150 nm)	HI-SCALE	(Koontz and Kuang, 2016)
Ultra-High Sensitivity Aerosol Spectrometer (UHSAS)	Ground, aircraft, ship	Aerosol size distribution (60 – 1000 nm), number concentration	HI-SCALE, ACE-ENA, MAGIC, MARCUS, CSET, SOCRATES	HI-SCALE, MAGIC, MARCUS: (Koontz and Uin, 2018) ACE-ENA: (Uin et al., 2018) CSET: 10.5065/D65Q4T96 SOCRATES: 10.5065/D6M32TM9
Condensation particle counter (CPC)	Ground, aircraft, ship	Aerosol number concentration (> 10 nm)	HI-SCALE, ACE-ENA, MAGIC, MARCUS	HI-SCALE (ground): (Kuang et al., 2016) ACE-ENA (ground), MAGIC: (Kuang et al., 2018a) MARCUS: (Kuang et al., 2018b) HI-SCALE (aircraft): (ARM, 2016b) ACE-ENA (aircraft): (Mei, 2018)
Condensation particle counter – ultrafine (CPCU)	Ground, aircraft	Aerosol number concentration (> 3 nm)	HI-SCALE, ACE-ENA	HI-SCALE (ground): 10.5439/1046186 HI-SCALE (aircraft): (ARM, 2016b) ACE-ENA (aircraft): 10.5439/1440985
Condensation nuclei counter (CNC)	Aircraft	Aerosol number concentration (11–3000 nm)	CSET, SOCRATES	CSET: 10.5065/D65Q4T96 SOCRATES: 10.5065/D6M32TM9
Cloud condensation nuclei (CCN) counter	Ground, aircraft, ship	CCN number concentration (0.1% to 0.5% supersaturation* depending on the platform)	HI-SCALE, ACE-ENA, MAGIC, MARCUS, SOCRATES	HI-SCALE (ground), ACE-ENA (ground), MARCUS: 10.5439/1342133 MAGIC: 10.5439/1227964 SOCRATES: 10.5065/D6Z036XB HI-SCALE (aircraft): (ARM, 2016a)
Aerosol chemical speciation monitor (ACSM)	Ground	Aerosol composition	HI-SCALE, ACE-ENA	10.5439/1762267
Microwave radiometer (MWR)	Ground, ship	Liquid water path, precipitable water vapor	MAGIC, MARCUS	10.5439/1027369
Counterflow virtual impactor (CVI)	Aircraft	Separates large droplets or ice crystals	HI-SCALE, ACE-ENA, SOCRATES	HI-SCALE: (ARM, 2016a) ACE-ENA: 10.5439/1406248 SOCRATES: 10.5065/D6M32TM9
Fast integrated mobility	Aircraft	Aerosol size distribution (10 – 425 nm)	HI-SCALE, ACE-ENA	HI-SCALE: (ARM, 2017) ACE-ENA: (ARM, 2020)



spectrometer (FIMS)				
Passive cavity aerosol spectrometer (PCASP)	Aircraft	Aerosol size distribution (120 – 3000 nm)	HI-SCALE, ACE-ENA, CSET	HI-SCALE: (ARM, 2016a) ACE-ENA: (ARM, 2018) CSET: 10.5065/D65Q4T96
Optical particle counter (OPC)	Aircraft	Aerosol size distribution (390 – 15960 nm)	ACE-ENA	(ARM, 2018)
Interagency working group for airborne data and telemetry systems (IWG)	Aircraft	Navigation information and atmospheric state parameters	HI-SCALE, ACE-ENA	HI-SCALE: (ARM, 2017) ACE-ENA: (ARM, 2018)
High-resolution time-of-flight aerosol mass spectrometer (AMS)	Aircraft	Aerosol composition	HI-SCALE, ACE-ENA	HI-SCALE: (ARM, 2017) ACE-ENA: 10.5439/1468474
Water content measuring system (WCM)	Aircraft	Cloud liquid and total water content	HI-SCALE, ACE-ENA	HI-SCALE: (ARM, 2016a) ACE-ENA: 10.5439/1465759
Doppler lidar (DL)	Ground	Boundary layer height	HI-SCALE	10.5439/1726254

167 * for measured supersaturations (SS) that vary over time, a $\pm 0.05\%$ window is applied (e.g., 0.5% SS
 168 includes samples with SS between 0.45% and 0.55%).



169
 170 **Figure 3. An example of a mean aerosol number distribution merged from FIMS, PCASP and OPC**
 171 **instruments for ACE-ENA aircraft measurements on 29 June 2017.**

172



173 **2.2 Preprocessing of model output**

174 We configured the EAMv1 to follow the Atmospheric Model Intercomparison Project (AMIP) protocol
175 (Gates et al., 1999) with real-world forcings (e.g., greenhouse gases, sea surface temperature, aerosol
176 emissions, etc.). In this study, we run the model from 2012 to 2018, covering all six field campaign
177 periods introduced previously, with at an additional 10 months for model spin-up. For each simulation
178 year, we use the year 2014 emission data from CMIP6, since the emission data does not cover years after
179 2014. The simulated horizontal winds are nudged towards the Modern-Era Retrospective analysis for
180 Research and Applications, Version 2 (MERRA-2, Gelaro et al., 2017) with a relaxation time scale of 6
181 hours. Previous studies (Sun et al., 2019; Zhang et al., 2014) showed that with such nudging configuration
182 the large-scale circulation is well constrained in the nudged simulation, especially for the mid- and high-
183 latitude regions. The simulation uses a horizontal grid spacing of $\sim 1^\circ$ (NE30, the number of elements
184 along a cube face of the E3SM High-Order Methods Modeling Environment, HOMME, dynamics core)
185 with a 30-minute timestep. We saved hourly output to compare with field campaign measurements. The
186 diagnostics package post-processes 3-D model variables associated with aerosol concentration, size,
187 composition, optical properties, precursor concentration, CCN concentration, and atmospheric state
188 variables. The size of output data is reduced by saving 3-D variables only over the field campaign
189 regions.

190 We extracted model output along the aircraft (ship) tracks using an “aircraft simulator” (Fast et al.,
191 2011) strategy to facilitate comparisons of observations and model predictions. At each aircraft (ship)
192 measurement time, we find the nearest model grid cell, output time slice, and vertical level of the aircraft
193 altitude (or the lowest level for ship) to obtain the appropriate model values. Since there are both spatial
194 and temporal mismatch existing between model output and field measurements, the evaluation focuses on
195 overall statistics. We also calculate the aerosol size distribution from 1 nm to 3000 nm at 1 nm increments
196 from the individual size distribution modes in MAM4 to facilitate comparisons with observed aerosol
197 number distribution that has different size ranges for different instruments. All these variables are saved
198 in separate directories according to the specific aircraft (ship) tracks, as indicated in Figure 1.

199 **2.3 List of diagnostics and metrics**

200 Currently, ESMAC Diags produces the following diagnostics and metrics:

- 201 • Mean value, bias, RMSE and correlation of aerosol number concentration.
- 202 • Timeseries of aerosol variables (aerosol number concentration, aerosol number size distribution,
203 chemical composition, CCN number concentration) for each field campaign or intensive
204 observational period (IOP) at the surface or along each flight (ship) track.



- 205 • Diurnal cycle of aerosol variables at the surface.
- 206 • Mean aerosol number size distribution for each field campaign or IOP.
- 207 • Percentiles of aerosol variables by height for each field campaign or IOP.
- 208 • Percentiles of aerosol variables by latitude for each field campaign or IOP.
- 209 • Pie/bar charts of observed and predicted aerosol composition averaged over each field campaign
- 210 or IOP.
- 211 • Vertical profile of cloud fraction and LWC composite of aircraft measurements for each field
- 212 campaign or IOP.
- 213 • Timeseries of atmospheric state variables.
- 214 • Aircraft and ship track maps.

215

216 In the next section we will demonstrate these diagnostics and metrics by providing several examples.

217

218 **3. Examples**

219 Aerosol number concentration, size distribution, and chemical composition (that controls hygroscopicity)
220 are key quantities that impact aerosol-cloud interactions, such as the activation of cloud droplets. Errors in
221 model predictions of these aerosol properties contribute to uncertainties in aerosol direct and indirect
222 radiative forcing. These aerosol properties vary dramatically depending on location, altitude, season, and
223 meteorological conditions due to variability in emissions, formation mechanisms, and removal processes
224 in the atmosphere. This section shows some examples to illustrate the usage of this diagnostics package
225 on evaluating global models.

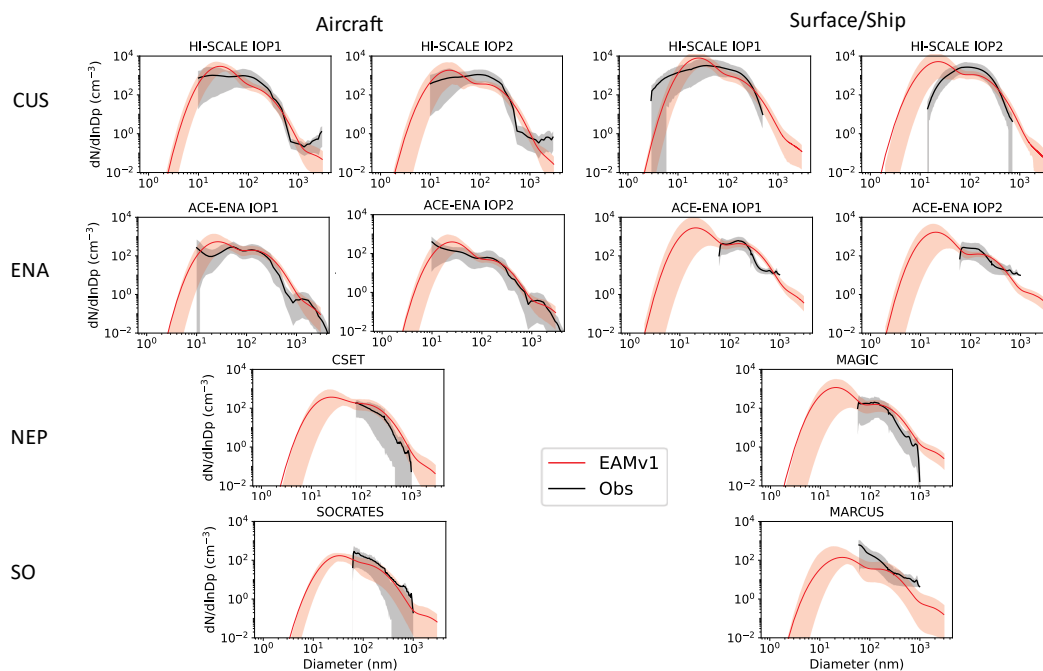
226 **3.1 Aerosol size distributions and number concentrations**

227 Aerosol properties are highly dependent on location and season. Figure 4 shows the mean aerosol size
228 distribution for each of the four testbed regions. For HI-SCALE and ACE-ENA, the two IOPs operated in
229 different seasons are shown separately. Table 3 shows the mean aerosol number concentration from these
230 field campaigns, for two particle size ranges: >10 nm and >100 nm. The 25% and 75% percentiles are
231 also shown to illustrate the variability in space and time. Among the four testbed regions, the CUS region
232 has the largest aerosol number concentrations since the other field campaigns are primarily over open
233 ocean. Overall, EAMv1 overestimates Aitken mode (10 – 70 nm) aerosols and underestimates
234 accumulation mode (70 – 400 nm) aerosols for the CUS and ENA regions, suggesting that processes
235 related to particle growth or coagulation might be too weak in the model. Over the NEP region, EAMv1
236 overestimates aerosol number for particle sizes >100 nm and >10 nm (Figure 4 and Table 3), both at the



237 surface and aloft. Over the SO region, which is considered a pristine region with low aerosol
 238 concentration, observations show a significant number of particles <200 nm in both aircraft and ship
 239 measurements. The mean aerosol number concentration over SO region is comparable or even greater
 240 than the other ocean testbeds (Table 3). In contrast, EAMv1 simulates a clean environment with the
 241 lowest aerosol number concentrations among the four regions. These types of comparisons demonstrate
 242 the need for additional analyses to understand why SO has more aerosols than other ocean regions and
 243 why EAMv1 cannot simulate this feature. The observed 75% percentiles are sometimes smaller than the
 244 mean value (Table 3), indicating skewed aerosol size distribution with long tail in large aerosol size.
 245 EAMv1 usually produces smaller range between 25% and 75% percentiles than the observations, likely
 246 because the current model resolution is too coarse to capture the observed spatial variability in aerosol
 247 properties.

248



249

250 **Figure 4: Mean aerosol number distribution averaged for each field campaign or IOP. Shadings**
 251 **denote the range between 10% and 90% percentiles.**



252 **Table 3: Mean aerosol number concentration and 25% and 75% percentiles (small numbers in**
 253 **parenthesis) for two size ranges averaged for each field campaign (or each IOP for HI-SCALE and**
 254 **ACE-ENA). Aircraft measurements 30 minutes after take-off and before landing are excluded to**
 255 **remove possible contamination from the airport.**

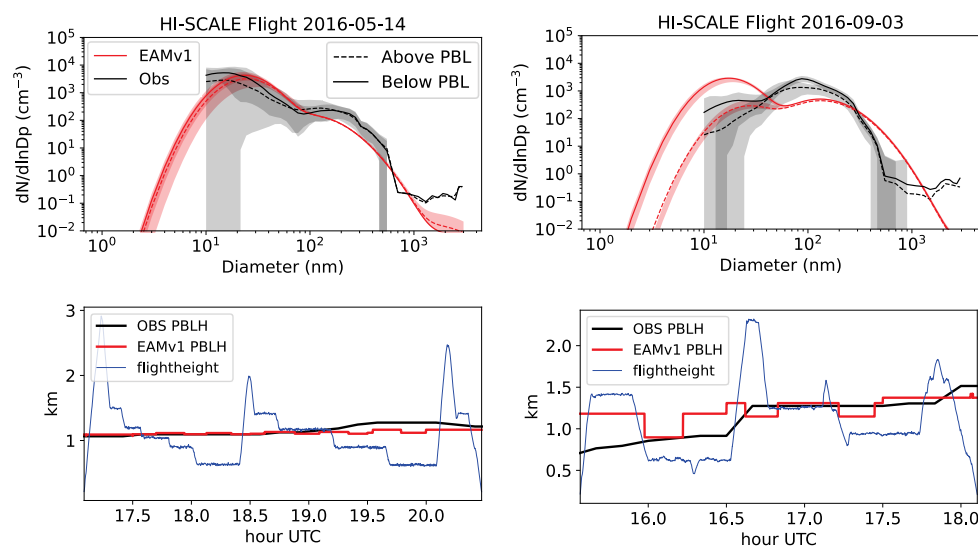
Unit: #/cm ³			>10 nm		>100 nm	
			CPC	E3SMv1	UHSAS/PCASP*	E3SMv1
CUS	Surface (HI-SCALE)	IOP1	4095 (2198, 4943)	4566 (2865, 5984)	675.1 (393.2, 929.5)	321.3 (229.7, 400.8)
		IOP2	N/A	N/A	N/A	N/A
	Aircraft (HI-SCALE)	IOP1	4206 (1132, 5013)	3872 (2803, 4946)	465.7 (112.6, 616.1)	159.6 (112.2, 200.5)
		IOP2	4121 (1610, 3829)	2514 (1332, 3584)	789.1 (444.4, 1088.0)	383.6 (280.7, 483.8)
ENA	Surface (ACE-ENA)	IOP1	610 (343, 711)	1723 (600, 1650)	206.1 (134.5, 267.1)	209.8 (155.3, 255.5)
		IOP2	458 (239, 505)	843 (320, 1152)	59.6 (25.0, 71.9)	61.9 (53.6, 71.9)
	Aircraft (ACE-ENA)	IOP1	576 (264, 677)	919 (562, 917)	135.6 (65.3, 185.1)	199.9 (146.6, 266.3)
		IOP2	356 (132, 383)	521 (279, 627)	72.8 (22.2, 72.8)	50.3 (41.6, 62.3)
NEP	Ship (MAGIC)	615 (116, 284)	1272 (357, 1646)	176.2 (65.3, 183.6)	246.4 (155.9, 273.9)	
	Aircraft (CSET)	408 (155, 386)	607 (353, 675)	81.5 (17.0, 73.4)	134.5 (81.2, 151.3)	
SO	Ship (MARCUS)	559 (270, 564)	324 (168, 318)	272.4 (72.5, 197.3)	107.8 (70.7, 128.3)	
	Aircraft (SOCRATES)	988 (327, 991)	237 (169, 270)	56.2 (14.1, 50.4)	32.3 (13.2, 42.2)	

256 * PCASP is used on aircraft for HI-SCALE and ACE-ENA. UHSAS is used for others.

257 Both observed and simulated aerosol size distribution and number concentration show large variability
 258 during these field campaigns. Over the period of a few weeks or longer, aerosol number can vary by an
 259 order of magnitude between the 10% and 90% percentiles, especially for small particles (Figure 4). Figure
 260 5 shows mean aerosol size distributions for two flight days during HI-SCALE: one with a large number of
 261 small (<70 nm) particles (14 May) and the other (3 September) with fewer small particles but more
 262 accumulation mode (70 – 300 nm) particles. On both days, EAMv1 reproduced the observed planetary
 263 boundary layer (PBL) height (PBLH) reasonably well with sufficient samples below and above PBL. On



264 14 May, EAMv1 reproduces the observed aerosol size distribution reasonably well both within the PBL
265 and in the lower free atmosphere. However, on 3 September EAMv1 produces too many aerosols in the
266 Aitken mode and too few accumulation mode aerosols in the PBL. In the free atmosphere, EAMv1
267 reproduces the lower concentration of Aitken mode aerosols but still underestimates the accumulation
268 mode. Such contrasting cases will be useful to help diagnose the specific processes contributing to model
269 uncertainties in future analyses. This large day-to-day variability also indicates that long-term
270 measurements are needed to avoid sampling bias in building robust statistics in aerosol properties. The
271 next version of ESMAC Diags will be extended to include the available long-term ARM measurements at
272 SGP, ENA and other sites outside of the field campaign time periods.



273
274 **Figure 5: (Top) Mean aerosol number distribution for two flights during HI-SCALE: (left) 14 May**
275 **2016 and (right) 3 September 2016, for data above (dashed line) and below (solid line) observed**
276 **PBLH. If there is cloud observed within a 1-hour window of the sample point, the above-PBL**
277 **sample needs to be above cloud top and the below-PBL sample needs to be below cloud base for the**
278 **sample point to be chosen. Shadings represent the data range between 10% and 90% percentiles.**
279 **Relatively large particles with no shading indicate more than 90% of samples with zero values.**
280 **(bottom) Timeseries of observed (black) and simulated (red) PBLH overlaid with flight height**
281 **(blue) during the two flight periods. The observed PBLH is derived from Doppler lidar**
282 **measurements.**

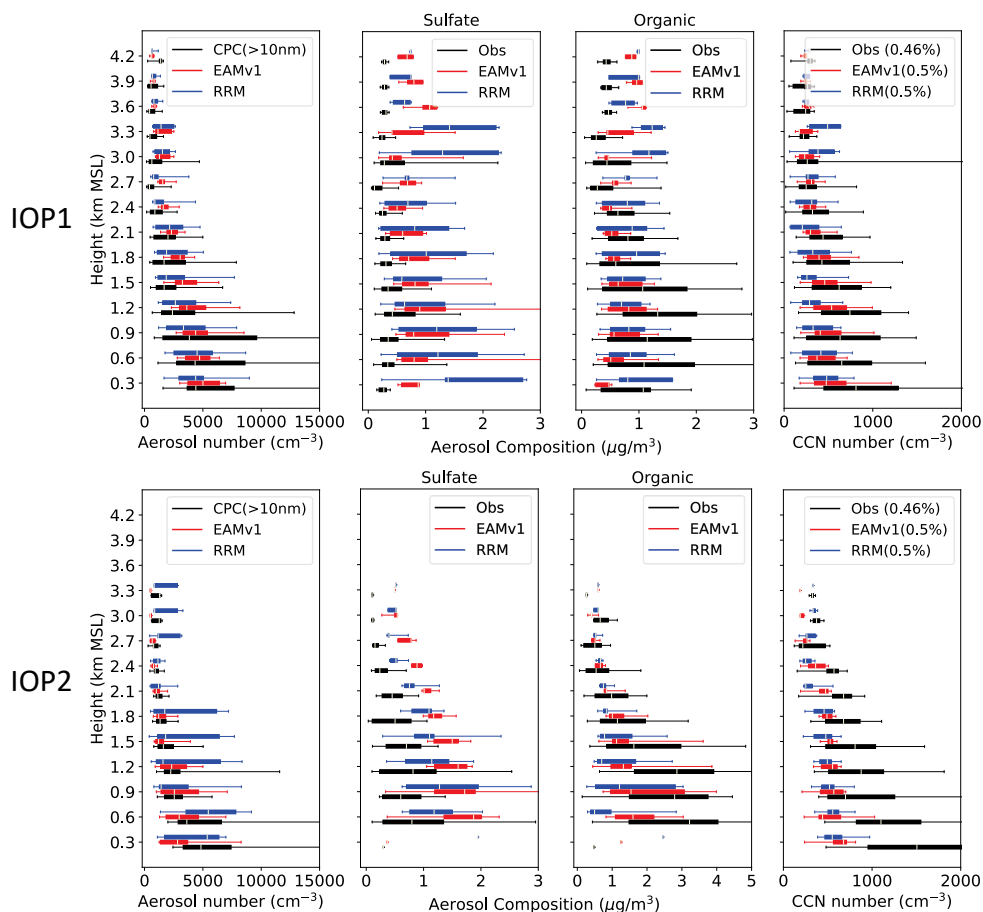
283



284 **3.2 Vertical profiles of aerosol properties**

285 A research aircraft is the primary platform to provide information on the vertical variations of key aerosol
286 properties that cannot be obtained accurately by remote sensing instrumentation. In this section we show
287 an example of evaluating vertical profiles of aerosol properties using aircraft measurements as well as
288 illustrate the capability of evaluating multiple model simulations with ESMAC Diags. In addition to the
289 standard EAMv1 simulation described in the previous section, we performed an EAMv1 simulation using
290 the regionally refined mesh (RRM) (Tang et al., 2019). The model is configured to run with the horizontal
291 grid spacing of $\sim 0.25^\circ$ over the continental U.S. and $\sim 1^\circ$ elsewhere. The two model configurations are
292 identical, except for the higher spatial resolution (including primary aerosol emissions) in the RRM over
293 the continental U.S. All aircraft measurements with a cloud detected simultaneously (cloud flag = 1) were
294 excluded.

295 Figure 6 shows vertical percentiles of aerosol number concentration, composition and CCN number
296 concentration among all the HI-SCALE aircraft flights. Note that aircraft rarely flew above 3 km during
297 HI-SCALE so the sample size above that altitude is much smaller. All observed aerosol properties
298 decrease with height since the major source of aerosols is from precursors emitted near the surface and
299 chemical formation within the PBL. EAMv1 generally simulates less variability than observations except
300 for sulfate. Overall, EAMv1 reproduces the observed mean aerosol number concentration for aerosol
301 size > 10 nm but underestimates the number of larger particles > 100 nm during HI-SCALE (Table 3).
302 The model also overestimates sulfate and underestimates organic matter concentrations when compared to
303 aircraft AMS measurements. Its underestimation of CCN number concentration is consistent with
304 underestimation of aerosol number concentration for diameter > 100 nm but contrary with overestimation
305 of sulfate. A similar relationship is seen for ACE-ENA, to be described later in this section.

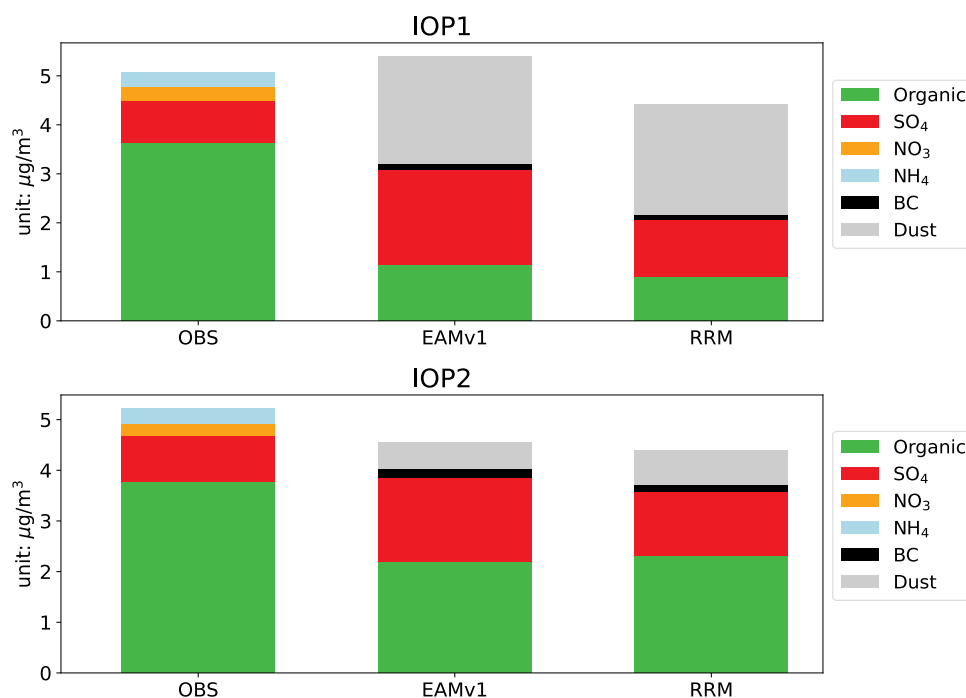


306

307 **Figure 6: Vertical profiles of (from left to right): aerosol number concentration, mass concentration**
 308 **of sulfate, mass concentration of total organic matter and CCN number concentration under the**
 309 **supersaturation in the parentheses for HI-SCALE (top) IOP1 and (bottom) IOP2. The percentile**
 310 **box represents 25% and 75% percentiles, and the bar represents 5% and 95% percentiles.**

311

312 The differences in sulfate and organic matter aloft is consistent with longer term surface measurement
 313 differences shown in Figure 7, suggesting this is a model bias. The greater fraction of sulfate in EAMv1
 314 suggests that the simulated aerosol hygroscopicity is likely higher than observed. Currently only these
 315 two species are available in both EAMv1 and AMS/ACSM observations for comparison purpose. Zaveri
 316 et al. (2021) recently added chemistry associated with NO₃ formation in MAM4, which is expected to be
 317 implemented in a future version of EAM.



318

319 **Figure 7: Bar plots of the surface average aerosol composition during HI-SCALE IOP1 (top) and**
320 **IOP2 (bottom). Observations are obtained from an ACSM. Dust and black carbon (BC) are not**
321 **measured in the observation. NO_3 and NH_4 are not predicted in EAMv1 and RRM.**

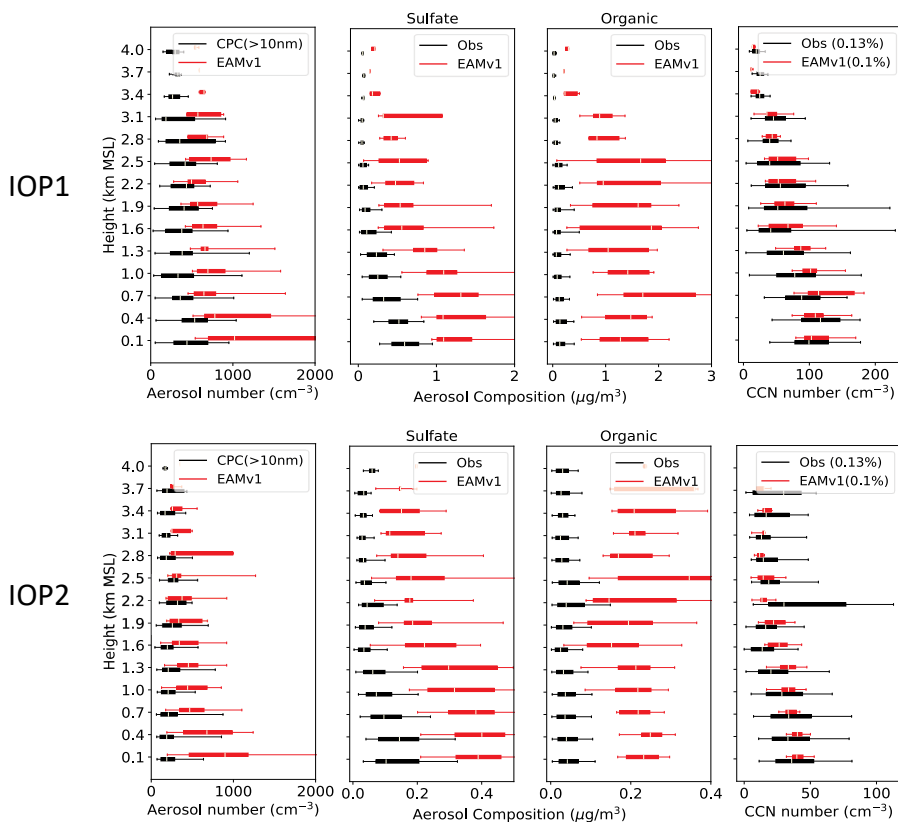
322 Ongoing developments in E3SM will soon permit regional-refined meshes with grid spacings as small
323 as ~ 3 km as well as global convection-permitting simulations ($\Delta x \sim 3$ km); therefore, this diagnostics
324 package is designed to be flexible in scale to take advantage of higher-resolution ESM simulations that
325 are more compatible with high-resolution in-situ aerosol observations. This study demonstrates this
326 ability by using a 0.25° RRM simulation. Overall, the RRM analyzed here has similar biases as EAMv1,
327 with differences that vary seasonally. The 25% to 75% percentiles in Figure 6 show that the variability of
328 organic aerosols and CCN from the EAMv1 and RRM simulations are similar. However, the variability of
329 sulfate in RRM is larger than EAMv1 and observations during the spring IOP (IOP1). During the summer
330 IOP (IOP2), the variabilities of sulfate in EAMv1, RRM, and observations are similar, and the sulfate
331 concentrations from RRM are closer to observed than EAMv1. Individual timeseries from the RRM
332 simulation are still too smooth to capture the fine scale variability of aerosols in observations (not shown).
333 We expect E3SM to capture more fine scale variabilities related to urban and point sources of aerosols
334 and their precursors when the simulation grid spacing is further reduced to ~ 3 km. A sensitivity study
335 will be conducted when this high-resolution version of E3SM simulation becomes available.



336 Figure 8 shows the vertical variation in percentiles of aerosol properties for ACE-ENA. The observed
337 aerosol number concentrations, composition masses, and CCN number concentrations are much smaller
338 than those for HI-SCALE, representing a cleaner ocean environment. EAMv1 produces larger mean
339 values than the observations for all these quantities. The overall variabilities in predicted aerosol number
340 and concentrations of sulfate and organic matter are also greater than observed. Note that the observed
341 variabilities for HI-SCALE are much larger than for ACE-ENA, indicating that EAMv1 has smaller
342 location variation on aerosol variabilities. The observed total organic concentration shows a peak aloft
343 between 1.6 and 2.2 km, corresponding to the level of CCN number concentration peak. This implies a
344 major source of aerosols or precursors is free tropospheric transport (Zawadowicz et al., 2021). This peak
345 of total organic concentration aloft is also captured by the model.

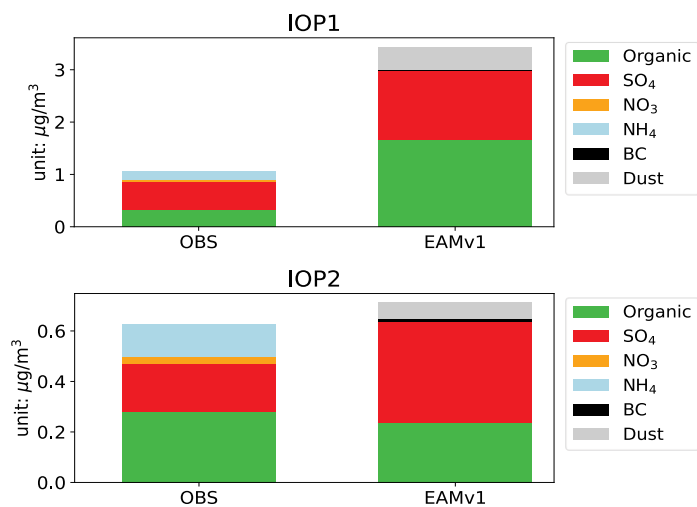
346 The bar plots in Figure 9 of aerosol composition at the surface during ACE-ENA from the ACSM
347 instrument and EAMv1 illustrate a similar bias in sulfate and organic mass as aloft. While the surface
348 sulfate measurements are like those from the aircraft at the lowest altitudes, the observed surface organic
349 matter is much higher than aloft, particularly during IOP2. The differences in these measurements may be
350 due to local effects or possible contamination from aircraft since the surface station is located near an
351 airport on an island.

352



353

354 **Figure 8:** Same as Figure 6 but for ACE-ENA.



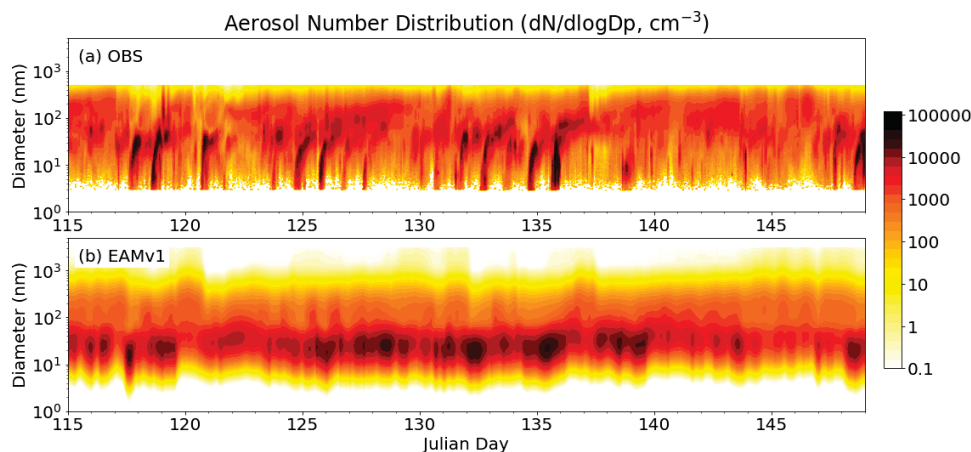
355

356 **Figure 9:** Same as Figure 7 but for ACE-ENA.



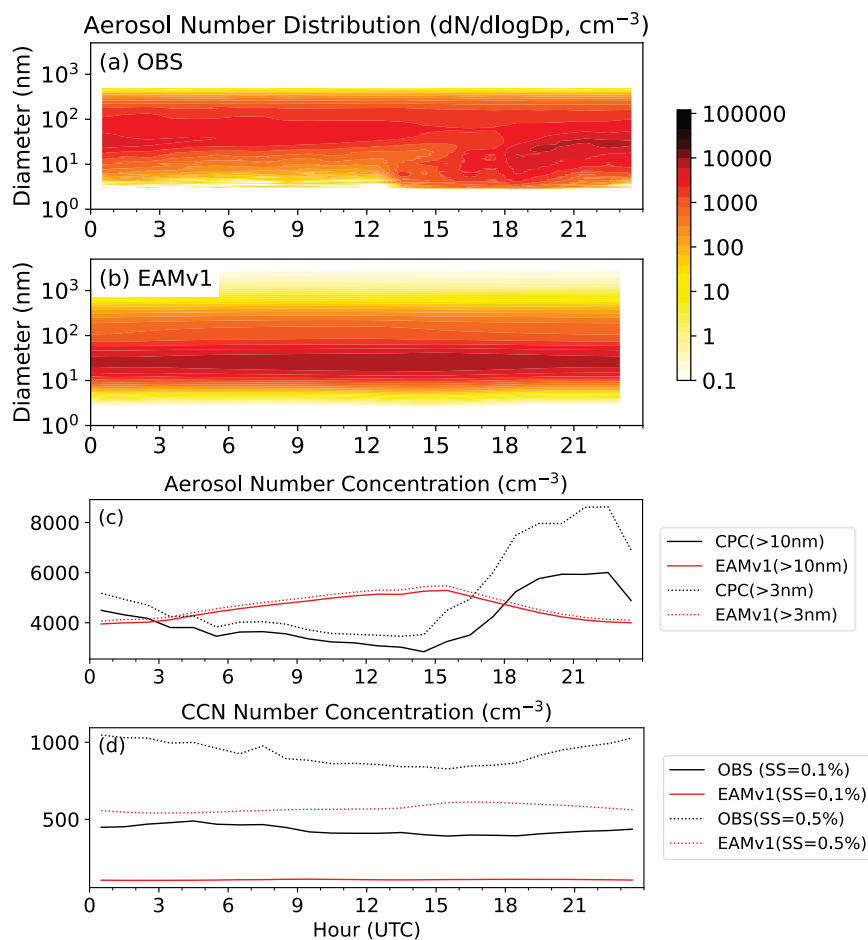
357 3.3 New particle formation events

358 Aerosol number concentrations and size distributions are highly impacted by new particle formation
359 (NPF) events (Kulmala et al., 2004), which further influence CCN concentration (e.g., Kuang et al., 2009;
360 Pierce and Adams, 2009) and ultimately cloud properties. NPF and subsequent particle growth are
361 frequently observed in the CUS region (Hodshire et al., 2016). As described by Fast et al. (2019) and
362 shown in Figure 10a, several NPF events were observed during the HI-SCALE spring IOP (IOP1). Large
363 concentrations of aerosols smaller than 10 nm were observed, with the size growing larger over the next
364 few hours. The average diurnal variation in aerosol number distribution in Figure 11a shows that NPF
365 events usually occur during the morning between 12 and 15 UTC (6 – 9 am local time), followed by
366 particle growth during the rest of the morning and afternoon. This variation is also seen in the diurnally
367 averaged CPC measurements of aerosol diameters > 3 nm and > 10 nm (Figure 11c) but diurnal changes
368 in CCN number concentrations (Figure 11d) are more modest.



369

370 **Figure 10: Time series of (a) observed and (b) simulated surface aerosol number distribution**
371 **during HI-SCALE IOP1. The observed aerosol number distribution is from merged nanoSMPS**
372 **and SMPS.**



373

374 **Figure 11: Average diurnal cycle of surface (a) observed aerosol number distribution, (b) simulated**
 375 **aerosol number distribution, (c) aerosol number concentration for diameters > 10 nm and > 3 nm,**
 376 **and (d) CCN number concentration for supersaturations of 0.1% and 0.5% for HI-SCALE IOP1.**

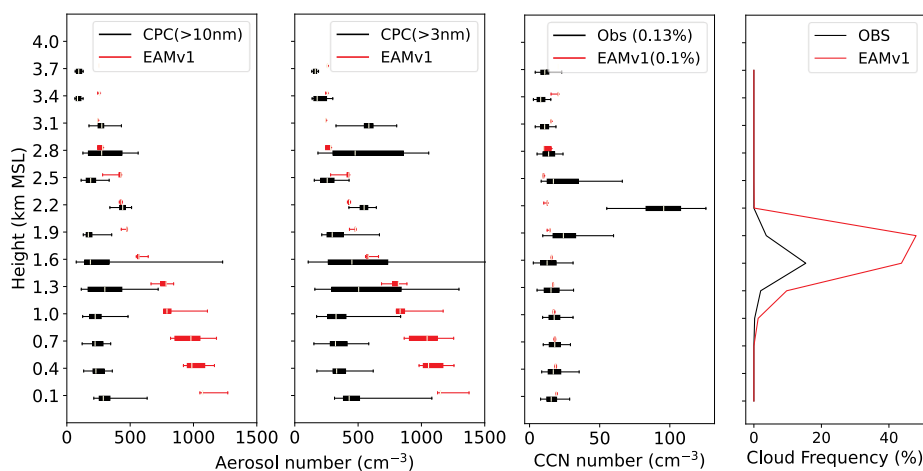
377

378 Various NPF pathways associated with different chemical species have been proposed and
 379 implemented in models. Two NPF pathways are considered in MAM4 in EAMv1: a binary nucleation
 380 pathway and a PBL cluster nucleation pathway. However, the current simulation does not reproduce the
 381 observed large day-to-day variability of small particle concentrations due to NPF. Instead, the model
 382 produces high aerosol concentrations between 10 and 100 nm almost all the time. It also fails to reproduce
 383 the large diurnal variability of aerosol and CCN number concentration with a peak seen in the morning
 384 near 15 UTC (9 am local time), 7 hours earlier than the observed 22 UTC (4 pm local time) afternoon



385 peak. Its overestimation of aerosol number concentration for particle diameter >10 nm and
386 underestimation of CCN number concentration is consistent with that shown in Figure 4. Several efforts
387 are underway to improve the simulation of NPF by adding a nucleation mode in MAM4 to explicitly
388 resolve ultrafine particles and implementing new chemical pathways to simulate NPF following Zhao et
389 al. (2020). ESMAC Diags is being used to evaluate these new model developments.

390 Using aircraft measurements from ACE-ENA, Zheng et al. (2021) recently found evidence of NPF
391 events occurring in the upper part of marine boundary layer between broken clouds following the passage
392 of a cold front. 16 February 2021 is identified as a typical NPF day in Zheng et al. (2021). The vertical
393 profiles of aerosol number and CCN concentrations measured by aircraft on 16 February 2018 are shown
394 in Figure 12. The NPF event and particle growth happened in the upper boundary layer is shown by the
395 large mean and variance of aerosol number concentration just below the base of the marine boundary
396 layer clouds. EAMv1 could not simulate NPF events in the upper marine boundary layer on this day and
397 other days during ACE-ENA, likely due to the lack of NPF mechanisms related to dimethyl sulfide
398 oxidation, and/or missing part in parameterizations to deal with the processes related to broken marine
399 boundary layer clouds and sub-grid circulation. Similarly, the sharp increase of CCN number just above
400 the level of marine boundary layer clouds is not simulated. The differences in observed and simulated
401 CCN suggests that simulated aerosol-cloud interactions are not likely to be representative even though the
402 simulated cloud height and depth agrees reasonably well with the aircraft measurements for this day.



403

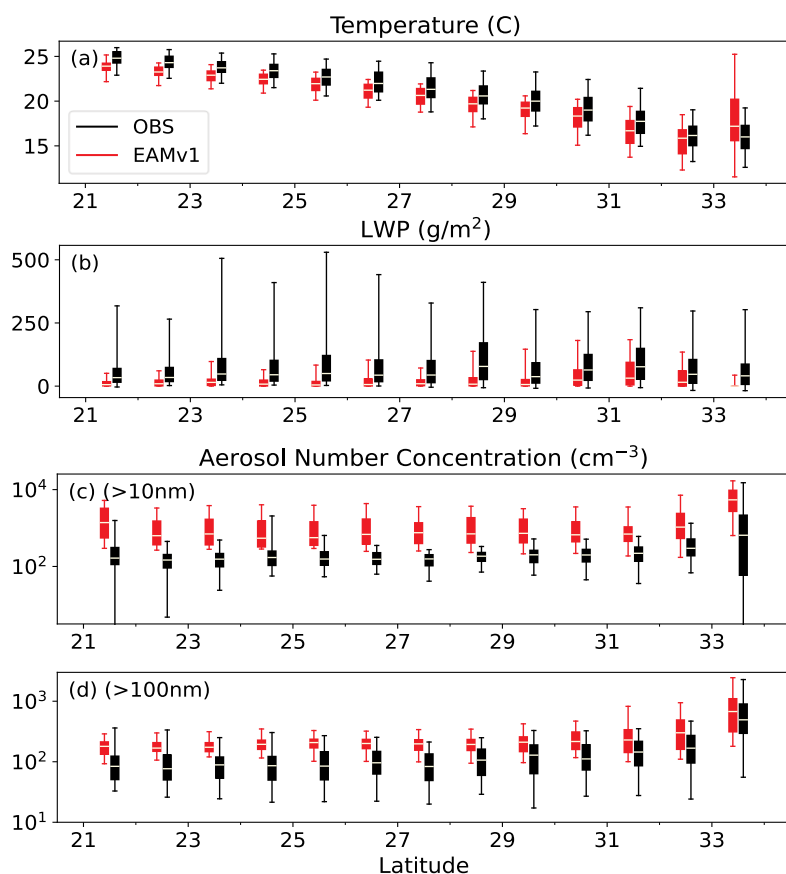
404 **Figure 12: Vertical profiles of aerosol number concentration for diameters >10 nm and >3 nm,**
405 **CCN number concentration, and cloud frequency measured by the 16 February 2018 flight in**
406 **ACE-ENA. The percentile box represents 25% and 75% percentiles, and the bar represents 5%**
407 **and 95% percentiles.**



408

409 3.4 Latitudinal dependence of aerosols and clouds

410 Unlike some field campaigns (i.e., HI-SCALE and ACE-ENA) where aircraft missions were conducted
411 over a relatively localized region with limited spatial variability of the meteorological conditions, ship
412 and/or aircraft measurements over the NEP and SO testbed regions span regions > 1500 km (i.e., from
413 California to Hawaii and from Tasmania to the far Southern Ocean, respectively). As shown in Figure 2,
414 there are large spatial gradients in EAMv1 simulated aerosol optical depth along these ship/aircraft tracks.
415 In ESMAC Diags version 1.0, we include composite plots of aerosol and cloud properties binned by
416 latitude to assess model representation of synoptic-scale variations.



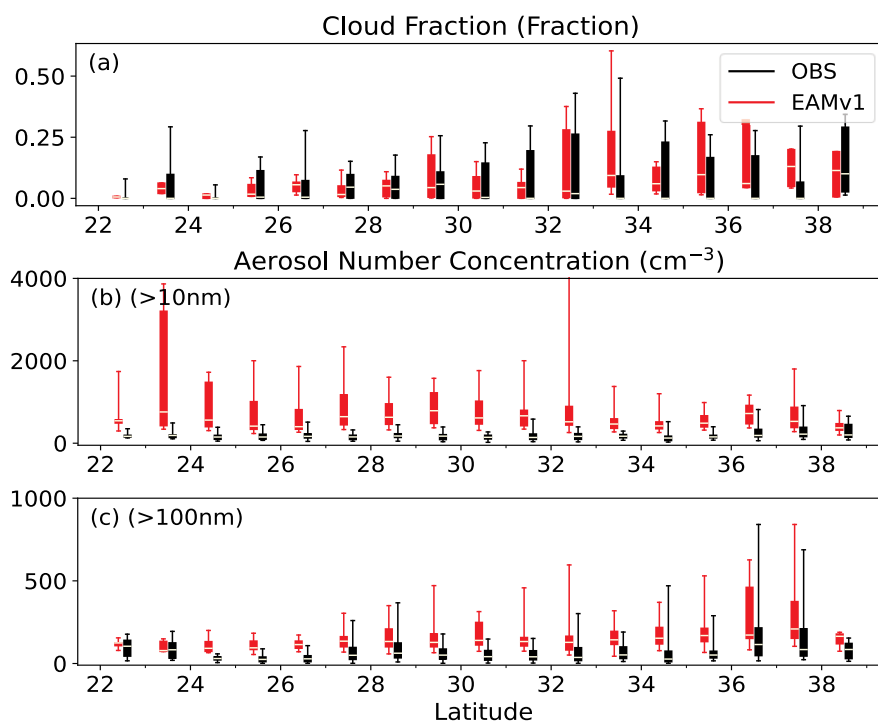
417

418 **Figure 13: Percentiles of (a) air temperature, (b) grid-mean liquid water path (LWP), (c) aerosol**
419 **number concentration for diameter >10 nm, and (d) aerosol number concentration for**
420 **diameter >100 nm for all ship tracks in MAGIC binned by 1° latitude bins. The percentile box**



421 represents 25% and 75% percentiles, and the bar represents 5% and 95% percentiles. The
422 observed aerosol number concentrations for diameters >10 nm and >100 nm are obtained from
423 CPC and UHSAS, respectively.

424



425

426 **Figure 14: Percentiles of (a) cloud fraction, (b) aerosol number concentration for diameter >10 nm,**
427 **and (c) aerosol number concentration for diameter >100 nm for all aircraft measurements between**
428 **0-3 km in CSET binned by 1° latitude bins. The percentile box represents 25% and 75%**
429 **percentiles, and the bar represents 5% and 95% percentiles. The observed aerosol number**
430 **concentrations for diameters >10 nm and >100 nm are obtained from CNC and UHSAS,**
431 **respectively.**

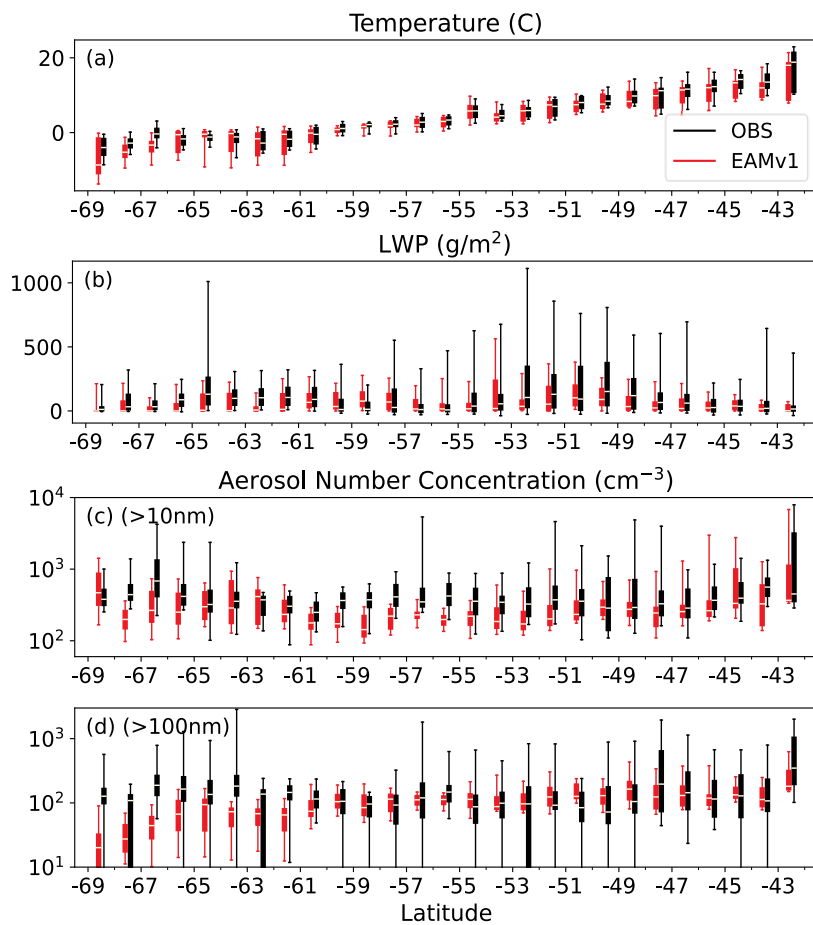
432

433 The research ship (aircraft) from the MAGIC (CSET) field campaign in the NEP testbed travelled
434 between California and Hawaii, where there is frequently a transition between marine stratocumulus
435 clouds near California and broken trade cumulus clouds near Hawaii (e.g., Teixeira et al., 2011). Some of
436 the meteorological, cloud, and aerosol properties along the ship (aircraft) tracks binned by latitude are



437 shown in Figure 13 (Figure 14). Note that cloud fraction in Figure 14 is calculated as cloud frequency in
438 aircraft observation and from grid-mean cloud fraction in model along the flight track. This is different
439 from the classic definition of cloud fraction usually used for satellite measurements or models and is
440 subject to aircraft sampling strategy. As the surface temperature decreases from Hawaii to California
441 (Figure 13a), the cloud fraction (Figure 14a) shows an increasing trend, indicating the transition from
442 marine cumulus to stratocumulus clouds. However, ship-measured LWP (Figure 13b) has no trend related
443 to latitude, possibly because cumulus clouds at lower latitudes have smaller cloud fraction but larger LWP
444 when clouds exist. EAMv1 shows increasing trends of both cloud fraction and LWP from low to high
445 latitudes along these tracks. It generally underestimates LWP and overestimates cloud fraction to the
446 north of 30° N. Additional cloud properties derived from surface and satellite measurements are not
447 included in the current analysis, which was constructed to focus on aerosols. They are planned to be
448 included in future versions. For aerosol number concentrations, EAMv1 produces too many aerosols
449 compared to measurements both at the surface (ship) and aloft (aircraft), consistent with the aerosol size
450 distribution in Figure 4 and total number concentration in Table 3. However, EAMv1 does reproduce the
451 increase trend in accumulation mode aerosol concentration approaching the California coast.

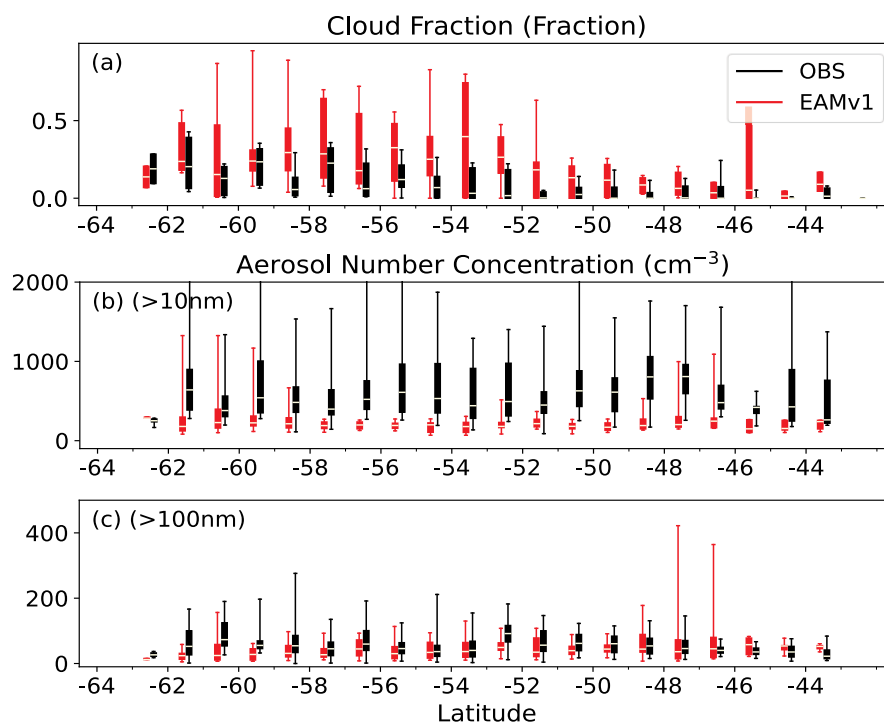
452 Similar plots along ship tracks from MARCUS and aircraft tracks from SOCRATES are shown in
453 Figures 15 and 16, respectively. Over the SO region, EAMv1 simulates smaller LWP (Figure 15b) but
454 higher cloud fraction (Figure 16a) than observations, similar to the biases seen over the NEP region.
455 Aerosols measured by ship and aircraft both show large variations in number concentration at any given
456 latitude bin over the campaign period, while EAMv1 generally produces lower mean concentrations and
457 smaller variability. This indicates that the physical and chemical processes related to aerosol lifetime over
458 the Southern Ocean need to be better understood and represented by EAMv1.



459

460 **Figure 15: Same as Figure 13 but for MARCUS.**

461



462

463 **Figure 16: Same as Figure 14 but for SOCRATES.**

464

465 4. Summary

466 A Python-based ESM aerosol-cloud diagnostics (ESMAC Diags) package is developed to quantify the
467 performance of the DOE's E3SM atmospheric model using ARM and NCAR field campaign
468 measurements. The first version of this diagnostics package focuses on aerosol properties. The
469 measurements include aerosol number, size distribution, chemical composition, and CCN collected from
470 surface, aircraft, and ship platforms needed to assess how well the aerosol lifecycle is represented across
471 spatial and temporal scales which will subsequently impact uncertainties in aerosol radiative forcing
472 estimates. Currently, the diagnostics cover the field campaigns of ACE-ENA, HI-SCALE,
473 MAGIC/CSET, and MARCUS/SOCRATES over Northeastern Atlantic, Continental U.S., Northeastern
474 Pacific, and Southern Ocean, respectively. The code structure is designed to be flexible and modular so
475 that evaluation against new field campaigns or additional datasets can be easily implemented. Since there
476 is no one instrument that can measure the entire aerosol size distribution, we have constructed merged
477 aerosol size distributions from two or more ARM instruments to better assess predicted size distributions.
478 An "aircraft simulator" is used to extract aerosol and meteorological model variables along flight paths



479 that vary in space and time. Similarly, the aircraft simulator is applied to ship tracks in which the altitude
480 remains fixed at sea level.

481 The version 1.0 of ESMAC Diags package can provide various types of diagnostics and metrics,
482 including timeseries, diurnal cycles, mean aerosol size distribution, pie charts for aerosol composition,
483 percentiles by height, percentiles by latitude, mean statistics of aerosol number concentration, and more.
484 A full set of diagnostics plots and metrics for simulations used in this paper are available at
485 https://portal.neresc.gov/project/m3525/sqtang/ESMAC_Diags_v1/forGMD/webpage/. This allows
486 quantification of model performance predicting aerosol number, size, composition, vertical distribution,
487 spatial distribution (along ship tracks or aircraft tracks) and new particle formation events. This paper
488 shows some examples to demonstrate the capability of ESMAC Diags to evaluate EAMv1 simulated
489 aerosol properties. The diagnostics package also allows multiple simulations in one plot to compare
490 different models or model versions. It can also be applied to evaluate other ESMs with small
491 modifications to process model output.

492 Because in-situ aerosol measurements are usually collected at high temporal frequency (typically 1
493 second to a minute) over fine spatial volumes, there is a spatiotemporal scale mismatch with the standard
494 climate model resolution (usually 1-degree grid spacing with hourly output). This is a limitation that
495 cannot be completely overcome and must be accepted to perform model-observation comparisons
496 necessary for identifying shortcomings in model representation of aerosol, cloud, and aerosol-cloud
497 interaction processes that are the primary source for uncertainties in prediction of future climate. As new
498 versions of E3SM become available that has grid spacings as small as a few kilometers via regional-
499 refined and convection-permitting global domains (e.g., Caldwell et al., 2021), spatiotemporal
500 variabilities of aerosols at finer scales should be captured and be more compatible with fine resolution
501 observations such that resolution impacts on statistical differences can be quantified. The diagnostics
502 package will be applied to diagnose high resolution model output when the data are available.

503 While the current version focuses on aerosol properties, a version 2 of ESMAC Diags is being planned
504 to include more diagnostics and metrics for cloud, precipitation, and radiation properties to facilitate the
505 evaluation of aerosol-cloud interactions. These include inversion strength, above cloud relative humidity,
506 cloud-surface coupling, cloud fraction, depth, LWP, optical depth, effective radius, droplet number
507 concentration, adiabaticity, and albedo, precipitation rate, and more. Analyses are being designed to
508 quantify relationships between these variables and relate them to effective radiative forcing, which will be
509 used to assess and improve model parameterizations. Additional surface-based and satellite retrievals will
510 also be used to address limitations related to data coverage and uncertainty. While there are other efforts
511 to develop model diagnostics packages, this diagnostics package provides a unique capability for detailed



512 evaluation of aerosol properties that are tightly connected with parameterized processes. Together with
513 other commonly used diagnostics packages such as the ARM diagnostics package (Zhang et al., 2020),
514 the DOE E3SM diagnostics package, and the PCMDI's metrics package (Gleckler et al., 2016), we expect
515 to better understand the strengths and weaknesses of E3SM or other ESMs and provide insights into
516 model deficiencies to guide future model development. This includes studies that develop a better
517 understanding of how various processes contribute to uncertainties in aerosol number and composition
518 predictions and subsequent representation of CCN and aerosol radiative forcing estimates.

519



520 **Code availability:**

521 *The current version of ESMAC Diags is publicly available through GitHub ([https://github.com/eagles-](https://github.com/eagles-project/ESMAC_diags)*
522 *[project/ESMAC_diags](https://github.com/eagles-project/ESMAC_diags)) under the new BSD license. The exact version (1.0.0-alpha) of the model used to*
523 *produce the results used in this paper is archived on Zenodo (<https://doi.org/10.5281/zenodo.5733233>).*

524 **Data availability:**

525 *Measurements from the HI-SCALE, ACE-ENA, MAGIC, and MARCUS campaigns as well as the SGP*
526 *and ENA sites are supported by the DOE Atmospheric Radiation Measurement (ARM) user facility and*
527 *available at <https://adc.arm.gov/discovery/>. Measurements from the CSET and SOCRATES campaigns*
528 *are supported by National Science Foundation (NSF) and obtained from NCAR Earth Observing*
529 *Laboratory at https://data.eol.ucar.edu/master_lists/generated/cset/ and*
530 *https://data.eol.ucar.edu/master_lists/generated/socrates/, respectively. DOI numbers or references of*
531 *individual instruments are given in Table 2. All the above observational data and preprocessed model*
532 *data used to produce the results used in this paper is archived on Zenodo*
533 *(<https://doi.org/10.5281/zenodo.5669136>).*

534 **Author contribution:**

535 *ST, JDF and PM designed the diagnostics package; ST wrote the code and performed the analysis; JES,*
536 *FM and MAZ processed the field campaign data; KZ contributed to the model simulation; JCH and ACV*
537 *contributed to the package design and setup; ST wrote the original manuscript; all authors reviewed and*
538 *edited the manuscript.*

539 **Competing interests:**

540 *Po-Lun Ma is a Topical Editor of Geoscientific Model Development. Other authors declare that they have*
541 *no conflict of interest.*

542 **Acknowledgements:**

543 *This study was supported by the Enabling Aerosol-cloud interactions at GLocal convection-permitting*
544 *scalES (EAGLES) project (74358), funded by the U.S. Department of Energy, Office of Science, Office of*
545 *Biological and Environmental Research, Earth System Model Development (ESMD) program area. We*
546 *thank the numerous instrument mentors for providing the data. This research used resources of the*
547 *National Energy Research Scientific Computing Center (NERSC), a U.S. Department of Energy Office of*
548 *Science User Facility operated under Contract No. DE-AC02-05CH11231. Pacific Northwest National*
549 *Laboratory (PNNL) is operated for DOE by Battelle Memorial Institute under contract DE-AC05-*
550 *76RL01830.*



551 **References:**

- 552 Albrecht, B., Ghate, V., Mohrmann, J., Wood, R., Zuidema, P., Bretherton, C., Schwartz, C., Eloranta, E.,
553 Glienke, S., Donaher, S., Sarkar, M., McGibbon, J., Nugent, A. D., Shaw, R. A., Fugal, J., Minnis, P.,
554 Palikonda, R., Lussier, L., Jensen, J., Vivekanandan, J., Ellis, S., Tsai, P., Rilling, R., Haggerty, J., Campos,
555 T., Stell, M., Reeves, M., Beaton, S., Allison, J., Stossmeister, G., Hall, S., and Schmidt, S.: Cloud System
556 Evolution in the Trades (CSET): Following the Evolution of Boundary Layer Cloud Systems with the NSF–
557 NCAR GV, Bull. Amer. Meteor. Soc., 100, 93-121, <https://doi.org/10.1175/bams-d-17-0180.1>, 2019.
- 558 Albrecht, B. A.: Aerosols, Cloud Microphysics, and Fractional Cloudiness, Science, 245, 1227-1230,
559 <https://doi.org/10.1126/science.245.4923.1227>, 1989.
- 560 AMWG Diagnostic Package: [https://www.cesm.ucar.edu/working_groups/Atmosphere/amwg-](https://www.cesm.ucar.edu/working_groups/Atmosphere/amwg-diagnosics-package/)
561 [diagnosics-package/](https://www.cesm.ucar.edu/working_groups/Atmosphere/amwg-diagnosics-package/), last access: 2 November 2021. 2021.
- 562 ARM Intensive Operational Period (IOP) Data Browser: [https://iop.archive.arm.gov/arm-](https://iop.archive.arm.gov/arm-iop/2012/mag/magic/reynolds-marmet/)
563 [iop/2012/mag/magic/reynolds-marmet/](https://iop.archive.arm.gov/arm-iop/2012/mag/magic/reynolds-marmet/), last access: 2 November 2021. 2014.
- 564 ARM Intensive Operational Period (IOP) Data Browser: [https://iop.archive.arm.gov/arm-](https://iop.archive.arm.gov/arm-iop/2016/sgp/hiscale/pekour-cvi)
565 [iop/2016/sgp/hiscale/pekour-cvi](https://iop.archive.arm.gov/arm-iop/2016/sgp/hiscale/pekour-cvi) last access: 2 November 2021. 2016a.
- 566 ARM Intensive Operational Period (IOP) Data Browser: [https://iop.archive.arm.gov/arm-](https://iop.archive.arm.gov/arm-iop/2016/sgp/hiscale/mei-cpc)
567 [iop/2016/sgp/hiscale/mei-cpc](https://iop.archive.arm.gov/arm-iop/2016/sgp/hiscale/mei-cpc), last access: 16 September 2021. 2016b.
- 568 ARM Intensive Operational Period (IOP) Data Browser: [https://iop.archive.arm.gov/arm-](https://iop.archive.arm.gov/arm-iop/2016/sgp/hiscale/shilling-ams)
569 [iop/2016/sgp/hiscale/shilling-ams](https://iop.archive.arm.gov/arm-iop/2016/sgp/hiscale/shilling-ams), last access: 2 November 2021. 2017.
- 570 ARM Intensive Operational Period (IOP) Data Browser: [https://iop.archive.arm.gov/arm-](https://iop.archive.arm.gov/arm-iop/2017/ena/aceena/mei-iwgl)
571 [iop/2017/ena/aceena/mei-iwgl](https://iop.archive.arm.gov/arm-iop/2017/ena/aceena/mei-iwgl), last access: 2 November 2021. 2018.
- 572 ARM Intensive Operational Period (IOP) Data Browser: [https://iop.archive.arm.gov/arm-](https://iop.archive.arm.gov/arm-iop/2017/ena/aceena/wang-fims/)
573 [iop/2017/ena/aceena/wang-fims/](https://iop.archive.arm.gov/arm-iop/2017/ena/aceena/wang-fims/), last access: 2 November 2021. 2020.
- 574 Caldwell, P. M., Terai, C. R., Hillman, B., Keen, N. D., Bogenschutz, P., Lin, W., Beydoun, H., Taylor,
575 M., Bertagna, L., Bradley, A. M., Clevenger, T. C., Donahue, A. S., Eldred, C., Foucar, J., Golaz, J.-C.,
576 Guba, O., Jacob, R., Johnson, J., Krishna, J., Liu, W., Pressel, K., Salinger, A. G., Singh, B., Steyer, A.,
577 Ullrich, P., Wu, D., Yuan, X., Shpund, J., Ma, H.-Y., and Zender, C. S.: Convection-Permitting Simulations
578 With the E3SM Global Atmosphere Model, Journal of Advances in Modeling Earth Systems, 13,
579 e2021MS002544, <https://doi.org/10.1029/2021MS002544>, 2021.
- 580 Campbell, J. R., Hlavka, D. L., Welton, E. J., Flynn, C. J., Turner, D. D., Spinhirne, J. D., Scott, V. S., III,
581 and Hwang, I. H.: Full-Time, Eye-Safe Cloud and Aerosol Lidar Observation at Atmospheric Radiation
582 Measurement Program Sites: Instruments and Data Processing, J. Atmos. Ocean. Technol., 19, 431-442,
583 [https://doi.org/10.1175/1520-0426\(2002\)019<0431:FTESCA>2.0.CO;2](https://doi.org/10.1175/1520-0426(2002)019<0431:FTESCA>2.0.CO;2), 2002.
- 584 Carslaw, K. S., Lee, L. A., Regayre, L. A., and Johnson, J. S.: Climate Models Are Uncertain, but We Can
585 Do Something About It, Eos, 99, <https://doi.org/10.1029/2018EO093757>, 2018.
- 586 E3SM Diagnostics: <https://e3sm.org/resources/tools/diagnostic-tools/e3sm-diagnostics/>, last access: 2
587 November 2021. 2021.



- 588 Eyring, V., Righi, M., Lauer, A., Evaldsson, M., Wenzel, S., Jones, C., Anav, A., Andrews, O., Cionni, I.,
589 Davin, E. L., Deser, C., Ehbrecht, C., Friedlingstein, P., Gleckler, P., Gottschaldt, K. D., Hagemann, S.,
590 Juckes, M., Kindermann, S., Krasting, J., Kunert, D., Levine, R., Loew, A., Mäkelä, J., Martin, G., Mason,
591 E., Phillips, A. S., Read, S., Rio, C., Roehrig, R., Senffleben, D., Sterl, A., van Ulft, L. H., Walton, J., Wang,
592 S., and Williams, K. D.: ESMValTool (v1.0) – a community diagnostic and performance metrics tool for
593 routine evaluation of Earth system models in CMIP, *Geosci. Model Dev.*, 9, 1747-1802,
594 <https://doi.org/10.5194/gmd-9-1747-2016>, 2016.
- 595 Fast, J. D., Gustafson, W. I., Chapman, E. G., Easter, R. C., Rishel, J. P., Zaveri, R. A., Grell, G. A., and
596 Barth, M. C.: The Aerosol Modeling Testbed: A Community Tool to Objectively Evaluate Aerosol Process
597 Modules, *Bull. Amer. Meteor. Soc.*, 92, 343-360, <https://doi.org/10.1175/2010bams2868.1>, 2011.
- 598 Fast, J. D., Berg, L. K., Alexander, L., Bell, D., D'Ambro, E., Hubbe, J., Kuang, C., Liu, J., Long, C.,
599 Matthews, A., Mei, F., Newsom, R., Pekour, M., Pinterich, T., Schmid, B., Schobesberger, S., Shilling, J.,
600 Smith, J. N., Springston, S., Suski, K., Thornton, J. A., Tomlinson, J., Wang, J., Xiao, H., and Zelenyuk,
601 A.: Overview of the HI-SCALE Field Campaign: A New Perspective on Shallow Convective Clouds, *Bull.*
602 *Amer. Meteor. Soc.*, 100, 821-840, <https://doi.org/10.1175/bams-d-18-0030.1>, 2019.
- 603 Gates, W. L., Boyle, J. S., Covey, C., Dease, C. G., Doutriaux, C. M., Drach, R. S., Fiorino, M., Gleckler,
604 P. J., Hnilo, J. J., Marlais, S. M., Phillips, T. J., Potter, G. L., Santer, B. D., Sperber, K. R., Taylor, K. E.,
605 and Williams, D. N.: An Overview of the Results of the Atmospheric Model Intercomparison Project
606 (AMIP I), *Bull. Amer. Meteor. Soc.*, 80, 29-56, [https://doi.org/10.1175/1520-0477\(1999\)080<0029:Aootro>2.0.Co;2](https://doi.org/10.1175/1520-0477(1999)080<0029:Aootro>2.0.Co;2), 1999.
- 608 Gelaro, R., McCarty, W., Suarez, M. J., Todling, R., Molod, A., Takacs, L., Randles, C., Darmenov, A.,
609 Bosilovich, M. G., Reichle, R., Wargan, K., Coy, L., Cullather, R., Draper, C., Akella, S., Buchard, V.,
610 Conaty, A., da Silva, A., Gu, W., Kim, G. K., Koster, R., Lucchesi, R., Merkova, D., Nielsen, J. E., Partyka,
611 G., Pawson, S., Putman, W., Rienecker, M., Schubert, S. D., Sienkiewicz, M., and Zhao, B.: The Modern-
612 Era Retrospective Analysis for Research and Applications, Version 2 (MERRA-2), *J. Climate*, 30, 5419-
613 5454, <https://doi.org/10.1175/JCLI-D-16-0758.1>, 2017.
- 614 Gleckler, P. J., Doutriaux, C., Durack, P. J., Taylor, K. E., Zhang, Y., Williams, D. N., Mason, E., and
615 Servonnat, J.: A more powerful reality test for climate models, *Eos, Trans. Amer. Geophys. Union*, 97,
616 <https://doi.org/10.1029/2016EO051663>, 2016.
- 617 Golaz, J.-C., Caldwell, P. M., Van Roekel, L. P., Petersen, M. R., Tang, Q., Wolfe, J. D., Abeshu, G.,
618 Anantharaj, V., Asay-Davis, X. S., Bader, D. C., Baldwin, S. A., Bisht, G., Bogenschutz, P. A., Branstetter,
619 M., Brunke, M. A., Brus, S. R., Burrows, S. M., Cameron-Smith, P. J., Donahue, A. S., Deakin, M., Easter,
620 R. C., Evans, K. J., Feng, Y., Flanner, M., Foucar, J. G., Fyke, J. G., Griffin, B. M., Hannay, C., Harrop, B.
621 E., Hoffman, M. J., Hunke, E. C., Jacob, R. L., Jacobsen, D. W., Jeffery, N., Jones, P. W., Keen, N. D.,
622 Klein, S. A., Larson, V. E., Leung, L. R., Li, H.-Y., Lin, W., Lipscomb, W. H., Ma, P.-L., Mahajan, S.,
623 Maltrud, M. E., Mametjanov, A., McClean, J. L., McCoy, R. B., Neale, R. B., Price, S. F., Qian, Y., Rasch,
624 P. J., Reeves Eyre, J. E. J., Riley, W. J., Ringler, T. D., Roberts, A. F., Roesler, E. L., Salinger, A. G.,
625 Shaheen, Z., Shi, X., Singh, B., Tang, J., Taylor, M. A., Thornton, P. E., Turner, A. K., Veneziani, M.,
626 Wan, H., Wang, H., Wang, S., Williams, D. N., Wolfram, P. J., Worley, P. H., Xie, S., Yang, Y., Yoon, J.-
627 H., Zelinka, M. D., Zender, C. S., Zeng, X., Zhang, C., Zhang, K., Zhang, Y., Zheng, X., Zhou, T., and
628 Zhu, Q.: The DOE E3SM Coupled Model Version 1: Overview and Evaluation at Standard Resolution, *J.*
629 *Adv. Model. Earth Syst.*, 11, 2089-2129, <https://doi.org/10.1029/2018ms001603>, 2019.
- 630 Hodshire, A. L., Lawler, M. J., Zhao, J., Ortega, J., Jen, C., Yli-Juuti, T., Brewer, J. F., Kodros, J. K.,
631 Barsanti, K. C., Hanson, D. R., McMurry, P. H., Smith, J. N., and Pierce, J. R.: Multiple new-particle



- 632 growth pathways observed at the US DOE Southern Great Plains field site, *Atmos. Chem. Phys.*, 16, 9321-
633 9348, <https://doi.org/10.5194/acp-16-9321-2016>, 2016.
- 634 Howie, J. and Kuang, C.: Scanning Mobility Particle Sizer (AOSSMPS) [dataset],
635 <https://doi.org/10.5439/1476898>, Accessed 14 January 2020.
- 636 IPCC, Stocker, T. F., Qin, D., Plattner, G.-K., Tignor, M., Allen, S. K., Boschung, J., Nauels, A., Xia, Y.,
637 Bex, V., and Midgley, P. M. (Eds.): *Climate Change 2013: The Physical Science Basis*. Contribution of
638 Working Group I to the Fifth Assessment Report of the Intergovernmental Panel on Climate Change,
639 Cambridge University Press, Cambridge, United Kingdom and New York, NY, USA, 1535 pp.,
640 <https://doi.org/10.1017/CBO9781107415324>, 2013.
- 641 Koontz, A. and Kuang, C.: Scanning mobility particle sizer (AOSNANOSMPS) [dataset],
642 <https://doi.org/10.5439/1242975>, Accessed 14 January 2020.
- 643 Koontz, A. and Uin, J.: Ultra-High Sensitivity Aerosol Spectrometer (AOSUHSAS) [dataset],
644 <https://doi.org/10.5439/1333828>, Accessed 3 February 2021.
- 645 Kuang, C., McMurry, P. H., and McCormick, A. V.: Determination of cloud condensation nuclei production
646 from measured new particle formation events, *Geophys. Res. Lett.*, 36,
647 <https://doi.org/10.1029/2009GL037584>, 2009.
- 648 Kuang, C., Salwen, C., and Singh, A.: Condensation Particle Counter (AOSPCF) [dataset],
649 <https://doi.org/10.5439/1046184>, Accessed 24 November 2020.
- 650 Kuang, C., Andrews, E., Salwen, C., and Singh, A.: Condensation Particle Counter (AOSPC) [dataset],
651 <https://doi.org/10.5439/1025152>, Accessed 16 September 2020.
- 652 Kuang, C., Salwen, C., Boyer, M., and Singh, A.: Condensation Particle Counter (AOSPCF1M) [dataset],
653 <https://doi.org/10.5439/1418260>, Accessed 3 February 2021.
- 654 Kulmala, M., Vehkamäki, H., Petäjä, T., Dal Maso, M., Lauri, A., Kerminen, V. M., Birmili, W., and
655 McMurry, P. H.: Formation and growth rates of ultrafine atmospheric particles: a review of observations,
656 *J. Aerosol Sci.*, 35, 143-176, <https://doi.org/10.1016/j.jaerosci.2003.10.003>, 2004.
- 657 Kyrouac, J. and Shi, Y.: Surface Meteorological Instrumentation (MET) [dataset],
658 <https://doi.org/10.5439/1786358>, Accessed 11 November 2020.
- 659 Lewis, E. R. and Teixeira, J.: Dispelling clouds of uncertainty, *Eos, Trans. Amer. Geophys. Union*, 96,
660 <https://doi.org/10.1029/2015eo031303>, 2015.
- 661 Liu, X., Ma, P. L., Wang, H., Tilmes, S., Singh, B., Easter, R. C., Ghan, S. J., and Rasch, P. J.: Description
662 and evaluation of a new four-mode version of the Modal Aerosol Module (MAM4) within version 5.3 of
663 the Community Atmosphere Model, *Geosci. Model Dev.*, 9, 505-522, [https://doi.org/10.5194/gmd-9-505-](https://doi.org/10.5194/gmd-9-505-2016)
664 [2016](https://doi.org/10.5194/gmd-9-505-2016), 2016.
- 665 Maloney, E. D., Gettelman, A., Ming, Y., Neelin, J. D., Barrie, D., Mariotti, A., Chen, C. C., Coleman, D.
666 R. B., Kuo, Y.-H., Singh, B., Annamalai, H., Berg, A., Booth, J. F., Camargo, S. J., Dai, A., Gonzalez, A.,
667 Hafner, J., Jiang, X., Jing, X., Kim, D., Kumar, A., Moon, Y., Naud, C. M., Sobel, A. H., Suzuki, K., Wang,
668 F., Wang, J., Wing, A. A., Xu, X., and Zhao, M.: Process-Oriented Evaluation of Climate and Weather



- 669 Forecasting Models, *Bull. Amer. Meteor. Soc.*, 100, 1665-1686, <https://doi.org/10.1175/bams-d-18-0042.1>,
670 2019.
- 671 McFarquhar, G. M., Bretherton, C. S., Marchand, R., Protat, A., DeMott, P. J., Alexander, S. P., Roberts,
672 G. C., Twohy, C. H., Toohey, D., Siems, S., Huang, Y., Wood, R., Rauber, R. M., Lasher-Trapp, S., Jensen,
673 J., Stith, J. L., Mace, J., Um, J., Järvinen, E., Schnaiter, M., Gettelman, A., Sanchez, K. J., McCluskey, C.
674 S., Russell, L. M., McCoy, I. L., Atlas, R. L., Bardeen, C. G., Moore, K. A., Hill, T. C. J., Humphries, R.
675 S., Keywood, M. D., Ristovski, Z., Cravigan, L., Schofield, R., Fairall, C., Mallet, M. D., Kreidenweis, S.
676 M., Rainwater, B., D'Alessandro, J., Wang, Y., Wu, W., Saliba, G., Levin, E. J. T., Ding, S., Lang, F.,
677 Truong, S. C. H., Wolff, C., Haggerty, J., Harvey, M. J., Klekociuk, A. R., and McDonald, A.: Observations
678 of Clouds, Aerosols, Precipitation, and Surface Radiation over the Southern Ocean: An Overview of
679 CAPRICORN, MARCUS, MICRE, and SOCRATES, *Bull. Amer. Meteor. Soc.*, 102, E894-E928,
680 <https://doi.org/10.1175/bams-d-20-0132.1>, 2021.
- 681 Mei, F.: Condensation particle counter for ACEENA [dataset], <https://doi.org/10.5439/1440985>, Accessed
682 5 December 2020.
- 683 Müller, D., Hostetler, C. A., Ferrare, R. A., Burton, S. P., Chemyakin, E., Kolgotin, A., Hair, J. W., Cook,
684 A. L., Harper, D. B., Rogers, R. R., Hare, R. W., Cleckner, C. S., Obland, M. D., Tomlinson, J., Berg, L.
685 K., and Schmid, B.: Airborne Multiwavelength High Spectral Resolution Lidar (HSRL-2) observations
686 during TCAP 2012: vertical profiles of optical and microphysical properties of a smoke/urban haze plume
687 over the northeastern coast of the US, *Atmos. Meas. Tech.*, 7, 3487-3496, <https://doi.org/10.5194/amt-7-3487-2014>, 2014.
- 689 Myhre, G., Samset, B. H., Schulz, M., Balkanski, Y., Bauer, S., Berntsen, T. K., Bian, H., Bellouin, N.,
690 Chin, M., Diehl, T., Easter, R. C., Feichter, J., Ghan, S. J., Hauglustaine, D., Iversen, T., Kinne, S.,
691 Kirkevåg, A., Lamarque, J. F., Lin, G., Liu, X., Lund, M. T., Luo, G., Ma, X., van Noije, T., Penner, J. E.,
692 Rasch, P. J., Ruiz, A., Seland, Ø., Skeie, R. B., Stier, P., Takemura, T., Tsigaridis, K., Wang, P., Wang, Z.,
693 Xu, L., Yu, H., Yu, F., Yoon, J. H., Zhang, K., Zhang, H., and Zhou, C.: Radiative forcing of the direct
694 aerosol effect from AeroCom Phase II simulations, *Atmos. Chem. Phys.*, 13, 1853-1877,
695 <https://doi.org/10.5194/acp-13-1853-2013>, 2013.
- 696 NETCDF: Introduction and Overview: <https://www.unidata.ucar.edu/software/netcdf/docs/index.html>, last
697 access: 2 November 2021. 2021.
- 698 Petters, M. D. and Kreidenweis, S. M.: A single parameter representation of hygroscopic growth and cloud
699 condensation nucleus activity, *Atmos. Chem. Phys.*, 7, 1961-1971, <https://doi.org/10.5194/acp-7-1961-2007>, 2007.
- 701 Pierce, J. R. and Adams, P. J.: Uncertainty in global CCN concentrations from uncertain aerosol nucleation
702 and primary emission rates, *Atmos. Chem. Phys.*, 9, 1339-1356, <https://doi.org/10.5194/acp-9-1339-2009>,
703 2009.
- 704 Rasch, P. J., Xie, S., Ma, P.-L., Lin, W., Wang, H., Tang, Q., Burrows, S. M., Caldwell, P., Zhang, K.,
705 Easter, R. C., Cameron-Smith, P., Singh, B., Wan, H., Golaz, J.-C., Harrop, B. E., Roesler, E., Bacmeister,
706 J., Larson, V. E., Evans, K. J., Qian, Y., Taylor, M., Leung, L. R., Zhang, Y., Brent, L., Branstetter, M.,
707 Hannay, C., Mahajan, S., Mامتjanov, A., Neale, R., Richter, J. H., Yoon, J.-H., Zender, C. S., Bader, D.,
708 Flanner, M., Foucar, J. G., Jacob, R., Keen, N., Klein, S. A., Liu, X., Salinger, A. G., Shrivastava, M., and
709 Yang, Y.: An Overview of the Atmospheric Component of the Energy Exascale Earth System Model, *J.*
710 *Adv. Model. Earth Syst.*, 11, 2377-2411, <https://doi.org/10.1029/2019ms001629>, 2019.



- 711 Reddington, C. L., Carslaw, K. S., Stier, P., Schutgens, N., Coe, H., Liu, D., Allan, J., Browse, J., Pringle,
712 K. J., Lee, L. A., Yoshioka, M., Johnson, J. S., Regayre, L. A., Spracklen, D. V., Mann, G. W., Clarke, A.,
713 Hermann, M., Henning, S., Wex, H., Kristensen, T. B., Leaitch, W. R., Pöschl, U., Rose, D., Andreae, M.
714 O., Schmale, J., Kondo, Y., Oshima, N., Schwarz, J. P., Nenes, A., Anderson, B., Roberts, G. C., Snider, J.
715 R., Leck, C., Quinn, P. K., Chi, X., Ding, A., Jimenez, J. L., and Zhang, Q.: The Global Aerosol Synthesis
716 and Science Project (GASSP): Measurements and Modeling to Reduce Uncertainty, *Bull. Amer. Meteor.*
717 *Soc.*, 98, 1857-1877, <https://doi.org/10.1175/bams-d-15-00317.1>, 2017.
- 718 Schulz, M., Textor, C., Kinne, S., Balkanski, Y., Bauer, S., Berntsen, T., Berglen, T., Boucher, O.,
719 Dentener, F., Guibert, S., Isaksen, I. S. A., Iversen, T., Koch, D., Kirkevåg, A., Liu, X., Montanaro, V.,
720 Myhre, G., Penner, J. E., Pitari, G., Reddy, S., Seland, Ø., Stier, P., and Takemura, T.: Radiative forcing by
721 aerosols as derived from the AeroCom present-day and pre-industrial simulations, *Atmos. Chem. Phys.*, 6,
722 5225-5246, <https://doi.org/10.5194/acp-6-5225-2006>, 2006.
- 723 Seinfeld, J. H., Bretherton, C., Carslaw, K. S., Coe, H., DeMott, P. J., Dunlea, E. J., Feingold, G., Ghan, S.,
724 Guenther, A. B., Kahn, R., Kraucunas, I., Kreidenweis, S. M., Molina, M. J., Nenes, A., Penner, J. E.,
725 Prather, K. A., Ramanathan, V., Ramaswamy, V., Rasch, P. J., Ravishankara, A. R., Rosenfeld, D.,
726 Stephens, G., and Wood, R.: Improving our fundamental understanding of the role of aerosol-cloud
727 interactions in the climate system, *Proc. Natl. Acad. Sci. U.S.A.*, 113, 5781-5790,
728 <https://doi.org/10.1073/pnas.1514043113>, 2016.
- 729 Sun, J., Zhang, K., Wan, H., Ma, P.-L., Tang, Q., and Zhang, S.: Impact of Nudging Strategy on the Climate
730 Representativeness and Hindcast Skill of Constrained EAMv1 Simulations, *J. Adv. Model. Earth Syst.*, 11,
731 3911-3933, <https://doi.org/10.1029/2019MS001831>, 2019.
- 732 Tang, Q., Klein, S. A., Xie, S., Lin, W., Golaz, J. C., Roesler, E. L., Taylor, M. A., Rasch, P. J., Bader, D.
733 C., Berg, L. K., Caldwell, P., Giangrande, S. E., Neale, R. B., Qian, Y., Riihimaki, L. D., Zender, C. S.,
734 Zhang, Y., and Zheng, X.: Regionally refined test bed in E3SM atmosphere model version 1 (EAMv1) and
735 applications for high-resolution modeling, *Geosci. Model Dev.*, 12, 2679-2706,
736 <https://doi.org/10.5194/gmd-12-2679-2019>, 2019.
- 737 Teixeira, J., Cardoso, S., Bonazzola, M., Cole, J., DelGenio, A., DeMott, C., Franklin, C., Hannay, C.,
738 Jakob, C., Jiao, Y., Karlsson, J., Kitagawa, H., Köhler, M., Kuwano-Yoshida, A., LeDrian, C., Li, J., Lock,
739 A., Miller, M. J., Marquet, P., Martins, J., Mechoso, C. R., Meijgaard, E. v., Meinke, I., Miranda, P. M. A.,
740 Mironov, D., Neggers, R., Pan, H. L., Randall, D. A., Rasch, P. J., Rockel, B., Rossow, W. B., Ritter, B.,
741 Siebesma, A. P., Soares, P. M. M., Turk, F. J., Vaillancourt, P. A., Von Engel, A., and Zhao, M.: Tropical
742 and Subtropical Cloud Transitions in Weather and Climate Prediction Models: The GCSS/WGNE Pacific
743 Cross-Section Intercomparison (GPCI), *J. Climate*, 24, 5223-5256, <https://doi.org/10.1175/2011jcli3672.1>,
744 2011.
- 745 Twomey, S.: The Influence of Pollution on the Shortwave Albedo of Clouds, *J. Atmos. Sci.*, 34, 1149-1152,
746 [https://doi.org/10.1175/1520-0469\(1977\)034<1149:TIOPOT>2.0.CO;2](https://doi.org/10.1175/1520-0469(1977)034<1149:TIOPOT>2.0.CO;2), 1977.
- 747 Uin, J., Senum, G., Koontz, A., and Flynn, C.: Ultra-High Sensitivity Aerosol Spectrometer (AOSUHSAS)
748 [dataset], <https://doi.org/10.5439/1409033>, Accessed 24 November 2020.
- 749 Wang, H., Easter, R. C., Zhang, R., Ma, P.-L., Singh, B., Zhang, K., Ganguly, D., Rasch, P. J., Burrows, S.
750 M., Ghan, S. J., Lou, S., Qian, Y., Yang, Y., Feng, Y., Flanner, M., Leung, R. L., Liu, X., Shrivastava, M.,
751 Sun, J., Tang, Q., Xie, S., and Yoon, J.-H.: Aerosols in the E3SM Version 1: New Developments and Their
752 Impacts on Radiative Forcing, *J. Adv. Model. Earth Syst.*, 12, e2019MS001851,
753 <https://doi.org/10.1029/2019ms001851>, 2020.



- 754 Wang, J., Wood, R., Jensen, M. P., Chiu, J. C., Liu, Y., Lamer, K., Desai, N., Giangrande, S. E., Knopf, D.
755 A., Kollias, P., Laskin, A., Liu, X., Lu, C., Mechem, D., Mei, F., Starzec, M., Tomlinson, J., Wang, Y.,
756 Yum, S. S., Zheng, G., Aiken, A. C., Azevedo, E. B., Blanchard, Y., China, S., Dong, X., Gallo, F., Gao,
757 S., Ghate, V. P., Glienke, S., Goldberger, L., Hardin, J. C., Kuang, C., Luke, E. P., Matthews, A. A., Miller,
758 M. A., Moffet, R., Pekour, M., Schmid, B., Sedlacek, A. J., Shaw, R. A., Shilling, J. E., Sullivan, A., Suski,
759 K., Veghte, D. P., Weber, R., Wyant, M., Yeom, J., Zawadowicz, M., and Zhang, Z.: Aerosol and Cloud
760 Experiments in the Eastern North Atlantic (ACE-ENA), *Bull. Amer. Meteor. Soc.*, 1-51,
761 <https://doi.org/10.1175/bams-d-19-0220.1>, 2021.
- 762 Watson-Parris, D., Schutgens, N., Reddington, C., Pringle, K. J., Liu, D., Allan, J. D., Coe, H., Carslaw, K.
763 S., and Stier, P.: In situ constraints on the vertical distribution of global aerosol, *Atmos. Chem. Phys.*, 19,
764 11765-11790, <https://doi.org/10.5194/acp-19-11765-2019>, 2019.
- 765 Winker, D. M., Vaughan, M. A., Omar, A., Hu, Y., Powell, K. A., Liu, Z., Hunt, W. H., and Young, S. A.:
766 Overview of the CALIPSO Mission and CALIOP Data Processing Algorithms, *J. Atmos. Ocean. Technol.*,
767 26, 2310-2323, <https://doi.org/10.1175/2009jtech1281.1>, 2009.
- 768 Zaveri, R. A., Easter, R. C., Singh, B., Wang, H., Lu, Z., Tilmes, S., Emmons, L. K., Vitt, F., Zhang, R.,
769 Liu, X., Ghan, S. J., and Rasch, P. J.: Development and Evaluation of Chemistry-Aerosol-Climate Model
770 CAM5-Chem-MAM7-MOSAIC: Global Atmospheric Distribution and Radiative Effects of Nitrate
771 Aerosol, *J. Adv. Model. Earth Syst.*, 13, e2020MS002346, <https://doi.org/10.1029/2020MS002346>, 2021.
- 772 Zawadowicz, M. A., Suski, K., Liu, J., Pekour, M., Fast, J., Mei, F., Sedlacek, A. J., Springston, S., Wang,
773 Y., Zaveri, R. A., Wood, R., Wang, J., and Shilling, J. E.: Aircraft measurements of aerosol and trace gas
774 chemistry in the eastern North Atlantic, *Atmos. Chem. Phys.*, 21, 7983-8002, <https://doi.org/10.5194/acp-21-7983-2021>, 2021.
- 776 Zhang, C., Xie, S., Tao, C., Tang, S., Emmenegger, T., Neelin, J. D., Schiro, K. A., Lin, W., and Shaheen,
777 Z.: The ARM Data-Oriented Metrics and Diagnostics Package for Climate Models: A New Tool for
778 Evaluating Climate Models with Field Data, *Bull. Amer. Meteor. Soc.*, 101, E1619-E1627,
779 <https://doi.org/10.1175/bams-d-19-0282.1>, 2020.
- 780 Zhang, K., Wan, H., Liu, X., Ghan, S. J., Kooperman, G. J., Ma, P. L., Rasch, P. J., Neubauer, D., and
781 Lohmann, U.: Technical Note: On the use of nudging for aerosol-climate model intercomparison studies,
782 *Atmos. Chem. Phys.*, 14, 8631-8645, <https://doi.org/10.5194/acp-14-8631-2014>, 2014.
- 783 Zhao, B., Shrivastava, M., Donahue, N. M., Gordon, H., Schervish, M., Shilling, J. E., Zaveri, R. A., Wang,
784 J., Andreae, M. O., Zhao, C., Gaudet, B., Liu, Y., Fan, J., and Fast, J. D.: High concentration of ultrafine
785 particles in the Amazon free troposphere produced by organic new particle formation, *Proc. Natl. Acad. Sci. U. S. A.*, 117, 25344-25351, <https://doi.org/10.1073/pnas.2006716117>, 2020.
- 787 Zheng, G., Wang, Y., Wood, R., Jensen, M. P., Kuang, C., McCoy, I. L., Matthews, A., Mei, F., Tomlinson,
788 J. M., Shilling, J. E., Zawadowicz, M. A., Crosbie, E., Moore, R., Ziemba, L., Andreae, M. O., and Wang,
789 J.: New particle formation in the remote marine boundary layer, *Nat. Commun.*, 12, 527,
790 <https://doi.org/10.1038/s41467-020-20773-1>, 2021.
- 791 Zhou, X., Kollias, P., and Lewis, E. R.: Clouds, Precipitation, and Marine Boundary Layer Structure during
792 the MAGIC Field Campaign, *J. Climate*, 28, 2420-2442, <https://doi.org/10.1175/jcli-d-14-00320.1>, 2015.

793